Search for New Physics in Events with a High Energy Photon, Electron and Large Missing Transverse Energy in pp Collisions at $\sqrt{s} = 8$ TeV

by

Aristotle Calamba

Submitted in partial fulfillment of the
requirements for the degree of
Doctor of Philosophy
at
Carnegie Mellon University
Department of Physics
Pittsburgh, Pennsylvania

Advised by Professor Manfred Paulini

September 24, 2014

Abstract

This thesis describes a search for new physics using data collected with the Compact Muon Solenoid experiment operating at the CERN Large Hadron Collider. The search was performed using events with a high energy photon, electron and large missing transverse energy. The data sample used in this analysis corresponds to an integrated luminosity of 19.6 fb^{-1} of proton-proton collisions at $\sqrt{s} = 8$ TeV produced at the Large Hadron Collider and collected by the CMS detector. The final state for this analysis is motivated by the theory of general gauge-mediated supersymmetry breaking but is also sensitive to any new physics producing massive particles with a photon and electron in the final state. The dominant standard model backgrounds to this search include quantum chromodynamics processes and electroweak processes involving $W^{\pm}$ bosons. An excess of events with large missing transverse energy as compared to the standard model expectation would indicate new physics. However, no excess of events is observed and the data is interpreted within a simplified supersymmetry model.

Acknowledgments

I would like to begin by thanking my Ph.D. advisor, Manfred Paulini, whose broad perspective and experience in high energy physics have greatly helped me at various stages of this thesis.

I want to thank the members of my thesis committee: James Russ, Roy Briere and Adam Leibovich for their comments and advice regarding my thesis.

I would like to thank Dongwook Jang and Soon Yung Jun for showing me the ropes of experimental high energy physics.

I would like to thank Yutaro Iiyama, without his help I would not be able to finish this thesis before my defense.

Lastly, I would to thank my wife, Gendith, and my parents for always reminding me to finish my thesis and move on with my life.

Contents

List of Tables

List of Figures

Chapter 1

Introduction

The standard model (SM) of particle physics is a fundamental and well-tested physics theory since its formulation. It has been extremely successful in describing existing experimental data. Many new particle discoveries were made largely because their existence was predicted by the standard model. Examples of such include, the discovery of the $W^{\pm}$ and Z bosons in the 1980's [1,2] and the discovery of the top quark in 1995 [3]. Another recent notable success is the discovery of the Higgs boson in 2012 [4, 5]. In addition, many of the SM's predictions could be experimentally verified to a high level of precision [6]. For example, the anomalous magnetic moment of the electron has been calculated to fourth loop order and agrees with the experimentally measured value up to ten significant figures [7, 8]. This is one of the most accurately verified predictions in physics.

Although high precision experiments have repeatedly confirmed subtle effects predicted by the SM, many unanswered fundamental physics questions are outside the realm of the SM. Furtheremore, there are several consequences of the standard model that lead to inconsistencies which are not yet resolved. For example, neutrinos are massless in the original SM framework. For these reasons, many physicists suggest

that there may be a more general theory that contains the standard model as a subset. One such theory is supersymmetry (SUSY).

This dissertation is an experimental search for physics beyond the standard model, motivated by the theory of supersymmetry. The search was performed on events with a high energy photon, electron and large missing transverse energy. The data sample used corresponds to an integrated luminosity of 19.6 fb^{-1} of proton-proton collisions at $\sqrt{s} = 8$ TeV collected by the Compact Muon Solenoid (CMS) detector at CERN's Large Hadron Collider (LHC).

This thesis is organized as follows. In Chapter 2, the standard model and the framework of supersymmetry motivating the analysis strategy of this thesis are discussed. In Chapter 3, the experimental layout of the LHC machine and the CMS detector are described. The dataset used in this analysis is outlined in Chapter 4. Chapter 5 covers the methods for identifying and reconstructing physical objects from the data. The analysis strategy and event selection is discussed in Chapter 6. The procedure for estimating the standard model background is detailed in Chapter 7. The result and summary of this work is presented in Chapter 8.

Chapter 2

Theoretical Framework and Motivation

In this chapter we will relate the standard model and supersymmetry as underlying theories to the experimental motivation and interpretation of this analysis. It is important to note that this discussion is not exhaustive but the SM and SUSY are just presented to the extent required to motivate the scope of this analysis.

2.1 Standard Model

The SM is a Yang-Mills gauge theory with the group structure

$$SU(3)_C \times SU(2)_L \times U(1)_Y. \tag{2.1}$$

Elementary particles are described as excitations of relativistic quantum fields. Particles with spin $\frac{1}{2}$ are called fermions. Interactions between fermions are mediated by exchanges of particles with spin 1, referred to as bosons. Three out of the four fun-

Table 2.1: Standard model's elementary fermions.

	Charge	1st Generation	2nd Generation	3rd Generation
Leptons	-1	e	μ	τ
	0	ν_e	ν_μ	ν_τ
Quarks	$+\frac{2}{3}$	u	c	t
	$-\frac{1}{3}$	d	s	b

damental interactions observed in nature are included in the SM, namely the strong, the weak and the electromagnetic interaction. A theory unifying gravity with the three interactions of the SM has not yet been established. Fermions are further classified as either leptons or quarks according to the different interactions in which they participate. Leptons and quarks are grouped into three generations. The first lepton generation consists of the electron e and the electron neutrino ν_e. The second and third generations are composed of the muon μ and muon neutrino ν_μ and the tau τ and tau neutrino ν_τ, respectively. The three lepton generations differ only in their masses and lifetimes. For example, the τ lepton can decay into final states containing muons or electrons but electrons are stable. Quarks are similarly divided into three generations. Each generation consists of an up-type quark with electric charge $+\frac{2}{3}$ and a down-type quark with electric charge -$\frac{1}{3}$. The first quark generation consists of the up quark u and down quark d. The second and third generations are composed of the charm quark c and strange quark s as well as the top quark t and bottom quark b, respectively. Table 2.1 shows a summary of the fermions of the SM.

Leptons are only subject to the electroweak interaction, which is accomplished under the symmetry group $SU(2)_L \times U(1)_Y$. Quarks on the other hand, carry color charge and can also interact via the strong force. Quantum chromodynamics (QCD) is the theory that describes the strong interaction and is based on the symmetry group $SU(3)_C$ [9, 10]. The quark fields are color triplets under the $SU(3)_C$ group

while leptons are color singlets. Gluons also carry a color charge which means that gluons can interact not only with quarks but also with other gluons. This is part of the reason for peculiar features, such as quark confinement and asymptotic freedom where the interactions between quarks and gluons become weaker as the distance between them decreases and the energy of the interaction increases.

First introduced by Glashow, Weinberg and Salam in 1967 [11–13], the $SU(2)_L \times U(1)_Y$ part of the SM symmetry group accounts for the electroweak interaction, the unified weak and electromagnetic force. The charges associated to these two symmetries are the weak isospin (T) and the weak hypercharge (Y). The associated gauge bosons fields of the electroweak symmetry are the isospin fields W_1, W_2 and W_3, while the corresponding hypercharge field is commonly denoted as B. Combinations of the W_1 and W_2 form the charged $W^{\pm}$ bosons that couple only to the left-handed helicity states of quarks and leptons. On the other hand, the linear combinations of W_3 and B form the Z boson and the photon γ:

$$\begin{pmatrix} \gamma \\ Z \end{pmatrix} = \begin{pmatrix} \cos\theta_W & \sin\theta_W \\ -\sin\theta_W & \cos\theta_W \end{pmatrix} \begin{pmatrix} B \\ W_3 \end{pmatrix} \tag{2.2}$$

where θ_W is the weak mixing angle, sometimes also called the Weinberg angle.

In the original $SU(2)_L \times U(1)_Y$ theory, SM particles including the gauge bosons are massless. Nonetheless, it is necessary to incorporate the concept of mass into the SM. Implicit mass terms for the electroweak bosons can be generated by introducing a scalar field and requiring it to have a non-zero vacuum expectation value. As a result the $SU(2)_L \times U(1)_Y$ symmetry is spontaneously broken [14], which does not only provide a mechanism to generate gauge boson masses, but also introduces an additional scalar particle, the Higgs boson. Elementary particles gain mass by

interacting with the Higgs boson, which is known as the Higgs mechanism. The Higgs boson was recently discovered in 2012 [4, 5] and found to have a mass of about 125 GeV.

2.2 Deficiencies of the Standard Model

Although the SM is a very successful theory and has been confirmed by experiments to a high level of precision up to the electroweak energy scale [6], there are plenty of motivations to explore particle physics beyond the SM. This section lists some of the open questions in the SM that motivates supersymmetric extensions.

2.2.1 Gravity

One of the most glaring shortcomings of the SM is the fact that gravity is not incorporated. The problem is not as important at low energies, since the gravitational interaction can be neglected as it is extremely weak compared to the other forces. However, for energies approaching the Planck scale ($M_p \sim 2.4 \times 10^{18}$ GeV) the strength of gravity is believed to be comparable to the other forces, making the SM invalid. Several theories beyond the standard model (BSM) aim to unify quantum theory with general relativity. The loop quantum gravity and superstring theory are examples of such theories [15, 16].

2.2.2 Gauge Coupling Unification

The $SU(3)_C \times SU(2)_L \times U(1)_Y$ gauge theory has three independent gauge coupling constants. The strength of the gauge couplings is dependent on the energy scale at which they are observed. This dependence is calculated using renormalization

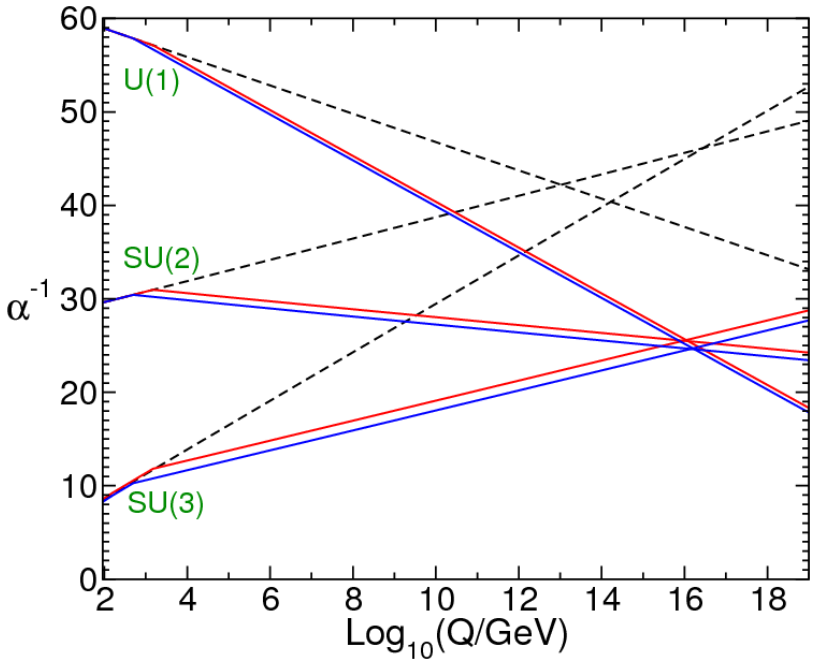

Figure 2.1: Evolution of the inverse gauge couplings $\alpha^{-1}(Q)$. The SM renormalization group evolution (dashed lines) is compared to the evolution in the Minimal Supersymmetric Standard Model (solid lines).

group equations. Under the SM, the extrapolation of the couplings to high energy scales does not result in their unification as displayed in Figure 2.1. However, under supersymmetric models this unification is realized with satisfactory accuracy [17]. The red and blue lines shown in the figure are found by varying supersymmetric particle masses between 500 and 1500 GeV and α_3, a SUSY parameter, between 0.117 and 0.121. In this case, the unification occurs at $\sim 2 \times 10^{16}$ GeV which is referred to as the Grand Unified Theory (GUT) scale.

2.2.3 Hierarchy Problem

The ratio of the GUT energy scale to the electroweak energy scale is huge. As a consequence, the Higgs boson mass, m_H, which is a free parameter in the SM

gets quadratically divergent loop corrections from all particles that couple to the Higgs field [18]. Fermions couple to the Higgs boson via the Yukawa term of the SM Lagrangian, $\lambda_f \bar{f} H f$, where λ_f is the Yukawa coupling and f is the fermion field. The one-loop correction to the Higgs mass due to fermions, as shown in Figure 2.2 (a), can be written as

$$\Delta m_H^2 = -\frac{|\lambda_f|^2}{8\pi^2}\Lambda^2 + \dots \tag{2.3}$$

where Λ is the cut-off scale. The largest correction comes from the top-quark which couples most strongly to the Higgs boson. If the SM is valid up to the Planck scale, ($\Lambda = M_p \sim 10^{19}$ GeV), Δm_H will be much larger than the Higgs boson mass, thus an unnatural fine tuning of the Higgs mass is needed in order to cancel the quadratically divergent corrections. However, if each fermion has a corresponding scalar superpartner, $\tilde{f}$, then these additional particles that also couple to the Higgs field would also contribute to the one-loop correction of the Higgs mass, as shown in Figure 2.2 (b). These contributions are given as

$$\Delta m_H^2 = \frac{|\lambda_{\tilde{f}}|^2}{8\pi^2}\Lambda^2 + \dots \tag{2.4}$$

The quadratic Λ term will cancel if $\lambda_f \approx \lambda_{\tilde{f}}$. The framework in which all SM particles have superpartners, the basic idea of supersymmetry, thus provides a way to avoid the hierarchy problem.

2.2.4 Dark Matter

Compelling evidence from astrophysical observations suggests the existence of dark matter in the universe. One example is the discrepancy between the observed galaxy rotational curves and the expected rotational curve based on the Newtonian theory

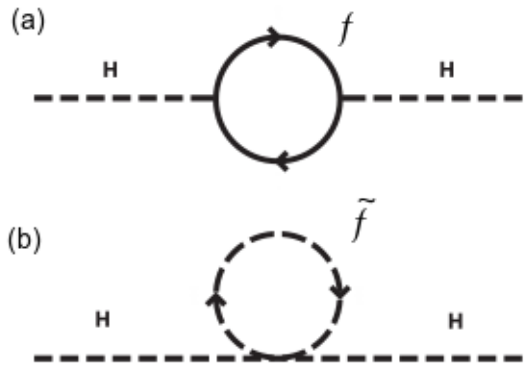

Figure 2.2: Feynman diagrams for the one-loop correction to the Higgs mass with (a) a fermion and (b) supersymmetric scalar.

of gravity [19]. The measured galactic rotation curve for NGC 6503, a dwarf spiral galaxy, is shown in Figure 2.3. As seen in the figure, the contributions made by the interstellar medium (gas) and the luminous matter in the galaxy is not enough to account for the observed rotational curve. A dark matter contribution has to be theorized in order to match the theoretical rotational curve to the observed one [20]. In addition, gravitational lensing studies of the Bullet Cluster show that much of its mass resides outside the central region of the baryonic mass [21].

The Wilkinson Microwave Anisotropy Probe (WMAP) estimates, by measuring the cosmic microwave background anisotropies, that baryonic matter constitutes only $\sim 4\%$ of the total mass and energy in the universe. The remaining $\sim 23\%$ and $\sim 73\%$ are attributed to dark matter and dark energy, respectively [22]. Until now, very litte is known about the nature of the last two components. Popular candidates for dark matter constituents are weakly interacting massive particles (WIMP), interacting only gravitationally and via the weak force, massive astrophysical compact halo object (machos) and axions. WIMPs naturally follow from many supersymmetric models.

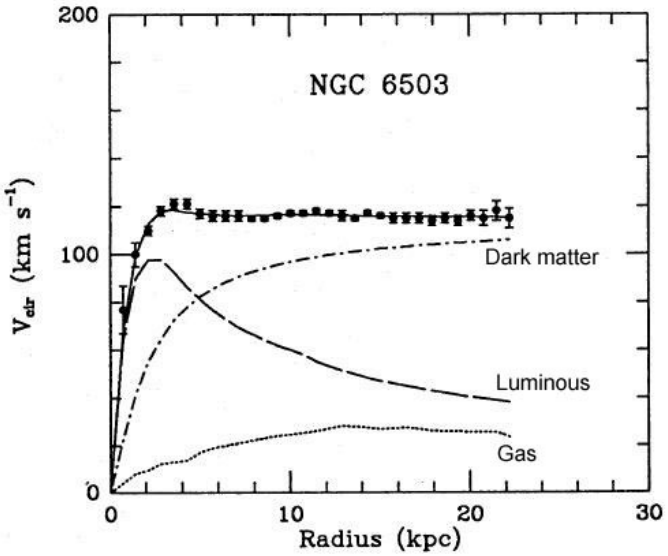

Figure 2.3: The dots with error bars represent the measured galactic rotation curve for NGC 6503. The overlapping solid line is the theoretical rotation curve. Also shown are the contributions made to the curve by gas, luminous matter, and dark matter.

2.3 Supersymmetry

Supersymmetry is a symmetry that relates fermions to bosons. A SUSY transformation converts a bosonic (fermionic) state into a fermionic (bosonic) state. The corresponding operator, S, transforms as the following:

$$S|\text{fermion}\rangle = |\text{boson}\rangle, \quad S|\text{boson}\rangle = |\text{fermion}\rangle. \tag{2.5}$$

A supermultiplet containing both fermion and boson states is an irreducible representation of single-particle states in a supersymmetric theory. Each supermultiplet has an equal number of fermionic and bosonic degrees of freedom. Supersymmetric partners of the SM fermions usually carry the same name but with a prefix "s" for scalar, (e.g. slepton or squark), while for superpartners of SM bosons it is common

to add the suffix "ino", (e.g. higgsino, wino, or gaugino).

Superpartners have identical mass and quantum numbers, except for their spin. The fact that no superpartner for any SM particle has been experimentally observed yet implies that the superpartners must be much heavier. Thus, SUSY must be a broken symmetry: SUSY particles have a larger mass than their SM counterpart. The origin of the supersymmetry breaking mechanism is unknown and often assumed to result from physics at a higher energy scale.

In the following sections, the simplest and best studied version of a realistic supersymmetric SM extension, the minimal supersymmetric standard model (MSSM) will be discussed.

2.3.1 Mimimal Supersymmetric Standard Model

Similar to the SM, its minimal supersymmetric extension, the MSSM [18,23,24] is also an $SU(3)_C \times SU(2)_L \times U(1)_Y$ gauge theory. It is a minimal extension with respect to the particle content, which is kept as small as possible. Each fermionic matter field of the SM is extended to a chiral supermultiplet by adding spin-0 scalar superpartners. It is important to note that the isospin structure of the SM is preserved in the MSSM. Hence, for every left-handed fermionic isospin doublet there is a supersymmetric isospin doublet, while SM isospin singlets have singlet supersymmetric counterparts. The bosonic gauge fields of the SM are extended to gauge supermultiplets with fermionic superpartners carrying spin $\frac{1}{2}$. The extension is straightforward for the gluons G_A (A $= 1 \ldots 8$), which are paired with gluinos $\tilde{G}_A$ to form supermultiplets. Table 2.2 shows the SM particles and their partners in the MSSM. Gluinos are color octet fermions, therefore they cannot mix with any other particle in the MSSM since there are no other fermionic color octets.

Table 2.2: SM particles and corresponding partners in the MSSM.

SM Particles		Spin	MSSM Particles		Spin
lepton	l	$1/2$	slepton	$\tilde{l}$	0
quark	q	$1/2$	squark	$\tilde{q}$	0
gluon	g	1	gluino	$\tilde{g}$	$1/2$
B boson	B	1	bino	$\tilde{B}$	$1/2$
W boson	$W^{\pm}, W^{o}$	1	wino	$\tilde{W^{\pm}}, \tilde{W^{o}}$	$1/2$
Higgs boson	H	1	higgsino	$\tilde{H}$	$1/2$

The situation is slightly more complicated for the superpartners of the electroweak gauge bosons, the winos $\tilde{W^a}$ and binos $\tilde{B}$. Like their SM counterparts, they mix because of the broken electroweak symmetry. But in contrast to the SM vector bosons, these states additionally mix with the fermionic components of the Higgs supermultiplets which consist of two complex Higgs doublets. The resulting mass eigenstates formed out of neutral higgsinos ($\tilde{H}_u^0, \tilde{H}_d^0$) and neutral gauginos ($\tilde{B}, \tilde{W}^0$) are called neutralinos ($\tilde{\chi}_i^0$, i = 1-4). The charged higgsinos ($\tilde{H}_u^+, \tilde{H}_d^-$) and charged gauginos ($\tilde{W}^1, \tilde{W}^2$) mix to form mass eigenstates called charginos ($\tilde{\chi}_i^{\pm}$, i = 1-2). The resulting gaugino mass eigenstates could be light enough to be produced and observed at the LHC.

Without other assumptions, the MSSM Lagrangian would contain terms that allow lepton (L) and baryon number (B) violating processes, like the decay of the proton to a lepton and a meson via a squark ($p^+ \rightarrow e^+\pi^0$). Proton decay, however, has never been observed experimentally and the lower limit on the proton lifetime is 6×10^{33} years [25]. There are no possible renormalizable Lagrangian terms that explicitly violate baryon or lepton conservation in the SM, thus it is not necessary to introduce any new fundamental symmetry as protection against such effects in the SM. Furthermore, it would be problematic to explicitly impose exact B or L conservation, since it is known

that both are violated by non-perturbative electroweak effects, although these effects are negligibly small [18, 26]. In order to protect the conservation of B and L in the MSSM, a new symmetry called R-parity is introduced [27–29]. It is a multiplicatively conserved quantum number and defined as

$$P_R = (-1)^{3(B+L)+2s} \tag{2.6}$$

where s denotes the spin. P_R is equal to 1 for all SM particles and -1 for SUSY particles. Other than the stability of the proton, R-parity conservation has the phenomenological consequence that only even numbers of supersymmetric particles can be produced in collider experiments. In addition, the decay products of supersymmetric particles must always comprise an odd number of lighter supersymmetric particles. This implies that the lightest supersymmetric particle (LSP) cannot decay solely to SM particles and is therefore stable. If the LSP is also electrically neutral, it can only interact weakly and gravitationally and thus matches all of the basic characteristics that are required of a dark matter candidate. An LSP could be observed indirectly by collider experiments through the momentum imbalance it causes when escaping the detector volume without interaction. Many searches for SUSY, including the one presented in this study, exploit this imbalance and are therefore mainly sensitive to R-parity conserving models. Despite these phenomenologically attractive implications, it has to be noted that R-parity conservation is not a mandatory requirement for extensions of the SM. In fact, it can be replaced by other mechanisms that satisfy the experimental constraints on B or L conservation. Such R-parity violating (RPV) models can exhibit decay topologies, substantially different to those considered in this thesis and therefore require other dedicated search strategies.

2.3.2 Gauge-Mediated SUSY Breaking

In the MSSM the particles in the same irreducible supermultiplet must have equal masses. However, no supersymmetric particle with the same mass as its SM partner has been discovered yet. With the energy scale at which modern accelarators are operating, SUSY particles should have been discovered if their masses are the same as their SM particle counterparts. Thus, for SUSY to exist, it must be a spontaneously broken symmetry. The idea of SUSY breaking is that there is a hidden sector in which SUSY is broken at some high-energy scale [30]. The breaking is mediated via messengers to a visible sector, which contains the MSSM. The mechanism by which this happens is still vigorously debated. There are several SUSY-breaking models depending on the type of mediation, the scale of the messenger mass and the SUSY breaking scale. Gravity is one possible method for breaking the symmetry. Another method is propagated by the ordinary gauge interactions. It is called the gauge-mediated supersymmetry breaking (GMSB). One important consequence of GMSB is that it solves the SUSY flavor problem of some SUSY-breaking models, e.g. the lepton-number violating decay $\mu \to e\gamma$ [31].

GMSB also provides a calculable and predictive framework and has a distinctive phenomenology which can be probed by modern particle colliders. The following are features that follow from GMSB and MSSM with R-parity [32–34]:

- SUSY particles will always be pair-produced.
- The lightest supersymmetric particle (LSP) is stable.
- The LSP must be the gravitino, $\tilde{G}$.
- The next-to-lightest supersymmetric particle (NLSP) always decays in a universal way to its SM superpartner plus the gravitino.

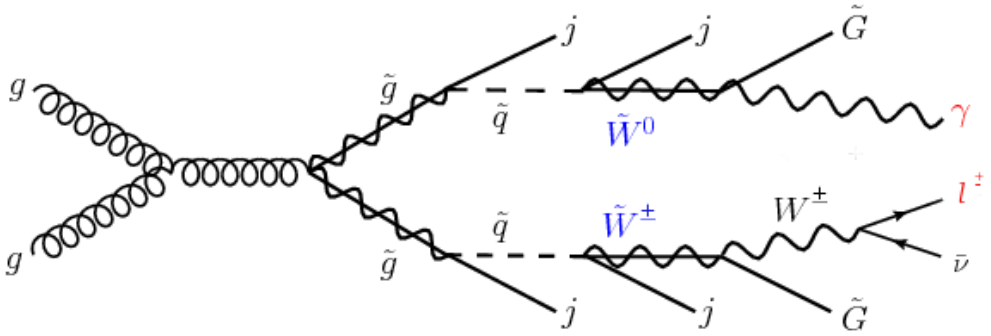

Figure 2.4: Feynman diagram of a GMSB wino-like neutralino process. Jets are represented as j.

- The lightest neutralino, $\tilde{\chi}_1^0$, and lightest chargino, $\tilde{\chi}_1^{\pm}$, are possible NLSP candidates.
- $\tilde{\chi}_1^0$ and $\tilde{\chi}_1^{\pm}$ have nearly degenerate mass when they are wino-like.
- The neutralino decays into a photon or a Z boson, $\tilde{\chi}_1^0 \rightarrow \gamma/Z + \tilde{G}$.
- The chargino decays into a W boson, $\tilde{\chi}_1^{\pm} \rightarrow W^{\pm} + \tilde{G}$.

These features can be illustrated in a Feynman diagram as shown in Figure 2.4. From this diagram we can see that an event described by GMSB and MSSM with R-parity is characterized by the presence of a photon and a lepton. Owing to its stability, the gravitino will not interact with the detector and escapes without detection. This effect can be detected by vectorially adding all transverse momenta of the objects reconstructed in the detector, looking for a momentum imbalance. The resulting imbalance in transverse momenta is referred to as missing transverse energy (E_T^{miss}). Figure 2.4 describes an event with high E_T^{miss} due to two high p_T gravitinos $\tilde{G}$ escaping the detector.

Therefore, events with a high p_T photon, an electron and large E_T^{miss}, detected in a collider detector could be events coming from GMSB with wino-like neutralinos.

This particular event scenario could also be achieved by standard model processes. As such, it is important to look for an excess of such GMSB events relative to the standard model prediction in order to claim evidence for a SUSY model based on GMSB and MSSM with R-parity and a wino-like neutralino and chargino.

Chapter 3

Large Hadron Collider and the Compact Muon Solenoid Detector

In this chapter, we will introduce the experimental apparatus used to gather the data utilized in this analysis: the Large Hadron Collider and the Compact Muon Solenoid detector.

3.1 The Large Hadron Collider

The Large Hadron Collider [35, 36] is a two-ring particle accelerator built by CERN, the European Organization for Nuclear Research. It lies in a 50-175-meter deep underground tunnel with a circumference of about 27 km at the border between Switzerland and France. The LHC is the highest energy particle accelerator in the world and is part of the CERN accelerator complex. Before protons are injected into the LHC, they are pre-accelerated to 450 GeV by an injector chain depicted in Figure 3.1.

The LHC consists of 1232 superconducting dipole magnets and 858 superconduct-

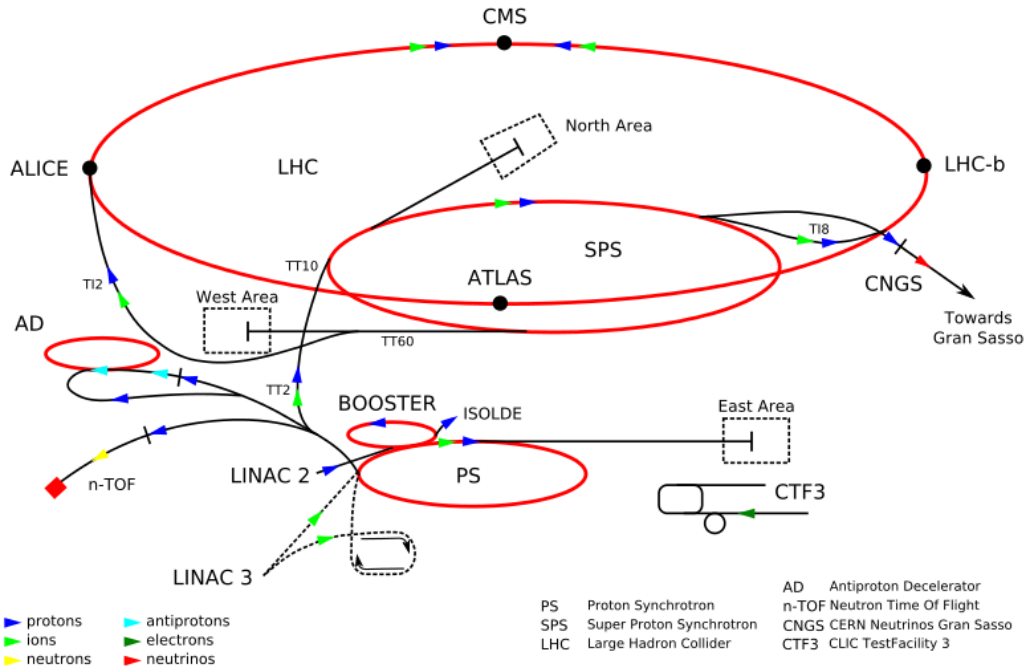

Figure 3.1: Schematic diagram of the LHC accelerator complex.

ing quadrupole magnets operated at a temperature of 1.9 K. At the maximum field strength of the dipole magnets, which is 8.36 T, protons can be accelerated up to 7 TeV. This corresponds to a center-of-mass energy $\sqrt{s}$ of 14 TeV for proton-proton collisions.

Proton beams in the LHC are structured into proton bunches with an approximate length of 8 cm. Each beam consists of up to 1380 bunches, with a bunch spacing of 50 ns. The design value for the instantaneous luminosity for proton-proton collisions is $L = 10^{34}$ cm^{-2}s^{-1}, which corresponds to about one billion proton-proton interactions per second. L is determined by the beam parameters,

$$L = \frac{N_b^2 \, n_b \, f_{rev} \, \gamma}{4\pi\epsilon_n \, \beta^*} F \tag{3.1}$$

where N_b denotes the number of particles per bunch, n_b the number of bunches per

Table 3.1: LHC key parameters.

Parameter	Unit	2010	2011	2012	Design
$\sqrt{s}$	GeV	7.0	7.0	8.0	14.0
N_p	10^{11} proton/bunch	1.2	1.5	1.6	1.15
n_b	bunch/beam	368	1380	1368,1374,1380	2808
Bunch spacing	ns	150	75, 50	50	25
ϵ_n	mm rad	2.4-4	1.9-2.4	2.2-2.5	3.75
β^*	m	3.5	1-1.5	0.6	0.55
peak L	10^{33} cm^{-1}s^{-1}	0.2	4	7.7	10

beam, f_{rev} the revolution frequency, γ the relativistic gamma factor, ϵ_n the normalized transverse beam emittance, β^* the beta function at the collision point and F the geometric luminosity reduction factor related to the crossing angle at the interaction point [36]. Table 3.1 lists the design parameters of the LHC and the corresponding values realized during the operation of the LHC from 2010 to 2012. The intensity per bunch has already exceeded the design value.

The rate dN/dt of a particle production process with a cross section σ is related to the luminosity by

$$\frac{dN}{dt} = L\sigma. \tag{3.2}$$

The integrated luminosity that quantifies the number of collisions is expressed as

$$\mathcal{L} = \int L dt = \frac{N}{\sigma}. \tag{3.3}$$

From this relation the actual expectation for the event count of any process can be calculated using its cross section.

Since the LHC became operational in 2009, its performance has continuously been increased towards the design values. In 2010, its center-of-mass energy was 7 TeV and it delivered an integrated luminosity of 47 pb^{-1}. In 2011, the peak instantaneous

luminosity reached 4.0 $\text{nb}^{-1}\text{s}^{-1}$, which is 40% of the design value. The LHC delivered an integrated luminosity of 6.1 fb^{-1} that year. The center-of-mass energy was increased to 8 TeV in 2012, reaching a peak instantaneous luminosity of 7.7 $\text{nb}^{-1}\text{s}^{-1}$. The LHC was able to deliver $\mathcal{L} = 23.3\ \text{fb}^{-1}$. It entered a two-year shutdown period as of February 2013. During this period, upgrades and improvements to the accelerator complex and the detectors will be employed in order to restart the LHC in 2015 at a center-of-mass energy close to the design $\sqrt{s} = 14$ TeV.

3.2 The Compact Muon Solenoid

The Compact Muon Solenoid is one of two multi-purpose experiments operating at the LHC. A detailed description of the CMS detector design, its physics goals and the computing environment necessary for its operation, can be found in the Technical Design Reports [37–39]. This section aims at giving a brief summary of the design and performance of CMS.

CMS is located approximately 100 meters below ground, at the LHC's interaction point 5 (see Figure 3.2). It is composed of various subdetector systems arranged in layers around the interaction region. The detector has a cylindrical shape with a length of 21.6 meters, a diameter of 14.6 meters and a total weight of 12,500 tons. A central component of the detector is its superconducting solenoidal magnet, which surrounds the silicon tracker as well as the electromagnetic and the hadronic calorimeters. The magnet itself is surrounded by a steel support structure which also serves as return yoke to ensure a homogeneous magnetic field inside the coil. This steel support structure holds the muon chambers which are mounted outside the calorimeters and the magnet. They are thereby shielded from all interacting particles except for muons. A schematic view of the CMS detector is shown in Figure 3.3

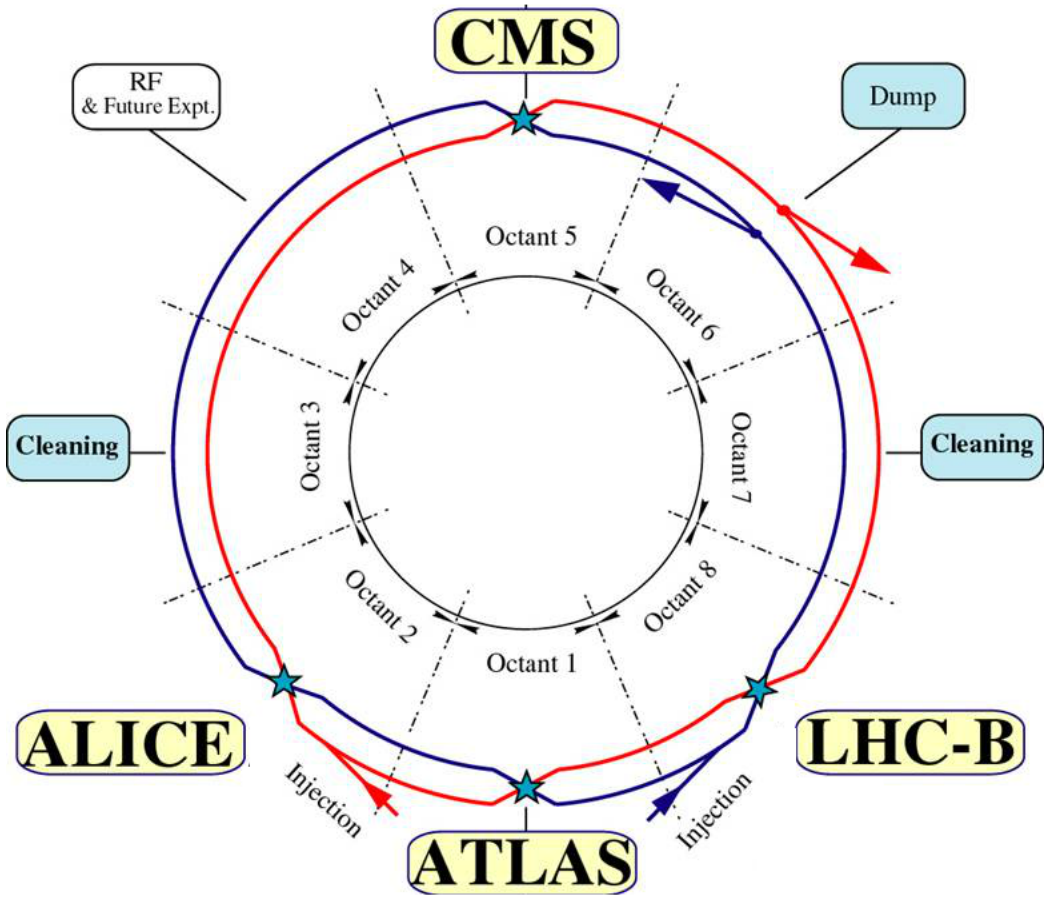

Figure 3.2: Schematic layout of the LHC ring.

3.2.1 Coordinate System

CMS uses a right handed coordinate system which has its origin at the geometric center of the detector, also referred to as the nominal beam spot. The true beam spot or interaction point does not necessarily coincide with the nominal beam spot due to the finite bunch length. The x-axis points towards the center of the LHC, the y-axis points upwards, and thus the z-axis points in the direction counterclockwise with respect to the LHC viewed from above. The azimuthal angle ϕ and the polar

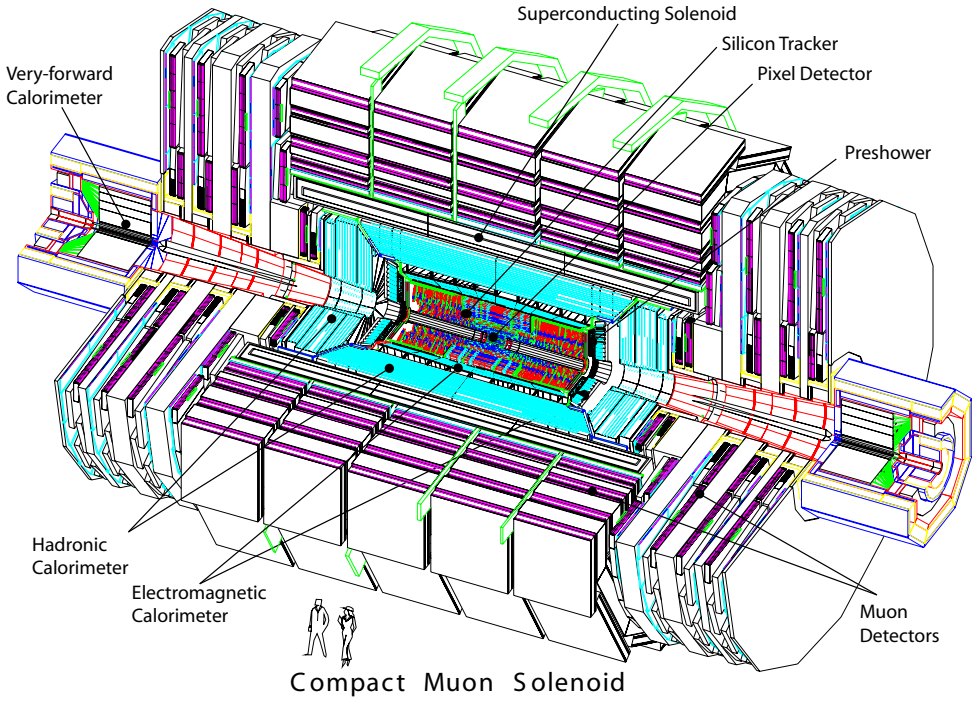

Figure 3.3: Diagram of the CMS detector.

angle θ are measured with respect to the x-axis and z-axis, respectively. Instead of the polar angle, it is convenient to use the pseudorapidity,

$$\eta = \frac{1}{2} \ln \left(\frac{|\vec{p}| + p_z}{|\vec{p}| - p_z} \right) = -\ln \left(\tan \left(\frac{\theta}{2} \right) \right) \tag{3.4}$$

a quantity that is numerically close to the relativistic rapidity, $y = \frac{1}{2} \ln \left(\frac{E+p_z}{E-p_z} \right)$, in the limit of high particle momenta $|\vec{p}| \gg m$. It has the advantage to be additive under Lorentz boosts. It is common to define a pseudo-angular distance ΔR between two directions (η_1, ϕ_1) and (η_2, ϕ_2) by

$$\Delta R_{12} = \sqrt{(\eta_1 - \eta_2)^2 + (\phi_1 - \phi_2)^2} = \sqrt{(\Delta\eta)^2 + (\Delta\phi)^2}. \tag{3.5}$$

3.2.2 Silicon Pixel Detector

The innermost detector system of CMS is the pixel detector. In the barrel region it consists of three cylindrical layers with a length of 53 cm at distances of 4.4 cm, 7.3 cm and 10.2 cm from the beam spot. These cylindrical layers are enclosed by two discs on each side positioned at $z = \pm 34.5$ cm and $z = \pm 46.5$ cm (see Figure 3.4). The pixel detector has 1440 sensor modules covering an active area of approximately 1 m^2. A single pixel has dimensions of 100×150 μm^2 which translates to approximately 66 million readout channels. The spatial resolution of 10-20 μm allows precise tracking of charged particles – an important ingredient for secondary particle decay vertex reconstruction and track seeding. An accurate and efficient reconstruction of secondary vertex positions facilitates the identification of heavy flavor production of top or bottom quarks, a capability which is crucial for the analysis of many physics processes.

Because of the proximity to the beam spot, the pixel sensors and readout chips are exposed to a high particle flux and are therefore designed to be resistant to damage caused by hard radiation. The lifetime of the innermost pixel layer is limited to 2-3 years, depending on the LHC's run conditions while the outermost layer is expected to operate for at least 10 years.

3.2.3 Silicon Strip Detector

The outer part of the CMS tracker consists of layers of silicon strip detectors arranged in four sections. The Tracker Inner Barrel (TIB) has four cylindrical layers at radii ranging from 25.5 cm to 49.8 cm. Toward the forward regions, the TIB is closed by the Tracker Inner Disks (TID) as shown in Figure 3.4. On each side, three discs are positioned between $|z| = 80$ cm and $|z| = 90$ cm. Together these two sections provide

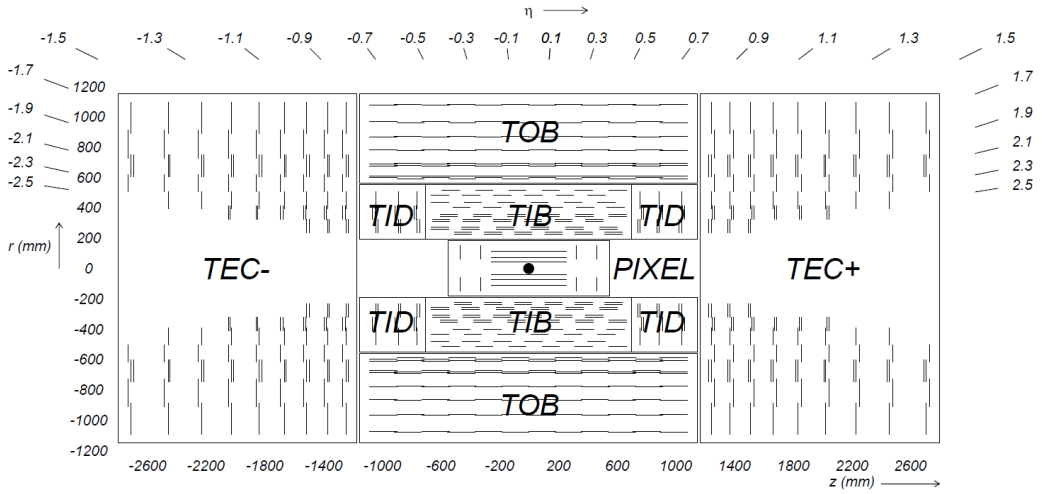

Figure 3.4: Schematic r-z view of the CMS tracker.

combined coverage up to $|\eta| = 2.2$. The outer two sections of the strip tracker are the Tracker Outer Barrel (TOB), which consist of six cylindrical detector layers and the Tracker End Caps (TEC) with nine discs on each end. The TEC increase the $|\eta|$ coverage to 2.5.

Several layers carry so called stereo modules composed of two sensors mounted back to back with a stereo angle of 100 mrad. These devices allow a measurement of the third coordinate (which is z for the barrel and r for the end cap sensors) and thus a 3-dimensional determination of a particle position. The spatial resolution of the TIB is 23-35 μm in ϕ and 230 μm in z. The TOB achieves resolutions of 35-52 μm in ϕ and 530 μm in z.

Like the pixel modules, the strip tracker is also radiation hard and operated at a temperature of 10^o C to minimize the effects of radiation damage. The tracker was designed to achieve a relative momentum resolution of less than 2% within $|\eta| < 1.6$ for muons at 100 GeV. For higher pseudorapidities the momentum resolution degrades, because of the reduced lever arm.

3.2.4 Electromagnetic Calorimeter

CMS utilizes a homogeneous electromagnetic calorimeter (ECAL), which consists of lead tungstate crystals ($PbWO_4$) as scintillator material. It is composed of a barrel ($|\eta| < 1.479$) and two encap regions ($1.479 < |\eta| < 3.0$). Avalanche photo diodes (APD's) are used to detect the scintillation photons in the barrel region, while vacuum photo triodes (VPT's), being more radiation hard than the silicon based APD's, are used for the endcaps. Lead tungstate was chosen as scintillator material, because it combines several favorable properties. Its high density (8.28 g/cm^3), short radiation length ($X_0 \sim 0.89$ cm) and small Moliere radius (2.2 cm) allow a fine granularity and a compact design of the calorimeter. The crystals in the barrel part have a depth of 23 cm, providing around 26 radiation lengths. Their front faces measure 22×22 mm^2 corresponding to $\Delta\eta \times \Delta\phi = 0.0175 \times 0.0175$ in the barrel region. The endcaps crystal size varies between 0.0175×0.0175 and 0.05×0.05 in η. Another favorable property of $PbWO_4$ is that it emits 80% of the scintillation photons within 25 ns and is therefore suitable for the high bunch crossing rates of 40 MHz.

The goal of the additional sampling calorimeter, the preshower detector, is to facilitate the identification of neutral pions and electrons. It is positioned in front of the endcaps and covers the pseudorapidity range $1.653 < |\eta| < 2.6$. It comprises two layers of lead and silicon strip sensors with a total thickness of 20 cm. The preshower detector adds $3X_0$ to the total radiation length of the ECAL endcaps.

Radiation damage also affects the performance of the ECAL. Ionizing radiation causes oxygen vacancies and lattice impurities, which change the transparency of the crystals, whereas the photon yield is not sensitive to irradiation. The loss of transparency is regularly measured by injecting laser light and is accounted for in the ECAL calibration.

A major design criteria for the ECAL was its ability to discover the Higgs boson in one of the most promising decay channels $H \to \gamma\gamma$. This requires a good mass resolution which is determined by the energy resolution of the ECAL. The energy resolution can be parametrized by

$$\frac{\sigma_E}{E} = \frac{S}{\sqrt{E(GeV)}} \oplus \frac{N}{\sqrt{E(GeV)}} \oplus C \tag{3.6}$$

up to energies of 500 GeV, where the shower leakage starts to become significant. The contributions to the resolution are parametrized by a stochastic term ($S = 2.8\%$), a noise term ($N = 0.12\%$) and a constant term ($C = 0.3\%$), dominant at high energies. Their values were determined from test beam measurements [70] and verified with collision data to fulfill the design goals.

3.2.5 Hadronic Calorimeter

The hadronic calorimeter (HCAL) of CMS was built as a non-compensating sampling calorimeter and consists of four elements. The barrel part (HB), fully contained inside the magnet coil, covers the pseudorapidity range $|\eta| < 1.3$. The endcaps (HE) cover $1.3 < |\eta| < 3.0$ and an additional forward calorimeter (HF) positioned at $|z| = 11.2$ m increases the calorimeter acceptance up to $|\eta| < 5$. Additional layers are mounted outside the magnet. These layers, which are called HCAL Outer (HO) calorimeters, serve as tail-catcher to ensure the containment of high energetic hadronic showers in the barrel region of $|\eta| < 1.3$. The HB alone provides only $5.82/\sin\theta$ interaction lengths (λ_I). Together with the ECAL barrel (providing $\sim 1.1\lambda_I$), the solenoid coil and the HO, the total depth of the calorimeter system is extended to a minimum of 11.8 interaction length in the barrel region. A schematic view of the hadronic calorimeter is shown in Figure 3.5. Except for the HF, where radiation hardness is

of prime importance, the HCAL consists of 5 cm thick layers of brass absorbers and plastic scintillators, which are read out with wave length shifting fibers connected to multichannel hybrid photo-diodes. Only the first and last layer of the HB are made of steel to increase the structural strength. The scintillators of the HB and the HO are divided into segments, covering $\Delta\eta\times\Delta\phi = 0.087\times0.087$ corresponding to a 5×5 cell of ECAL crystals. The same granularity is used in the HE for pseudo rapidities $|\eta| < 1.6$ while for $|\eta| > 1.6$ a coarser scintillator segmentation of $\Delta\eta \times \Delta\phi = 0.17 \times 0.17$ is in place.

The HF will suffer from the extremely high flux of high-energy particles. It is estimated that it will be exposed to $\sim$ 10 MGy during 10 years of LHC operation. To withstand these harsh conditions, absorber plates made of steel were chosen and quartz fibers are used as active material. They emit Cherenkov light when transversed by charged particles. Since the magnetic field strength in the forward region is smaller compared to the barrel region, conventional photomultiplier tubes are used for the HF to convert the optical signals.

The raw energy resolution measured for pions with momenta between 30 GeV and 300 GeV in the HCAL can be parametrized as

$$\frac{\sigma_E}{E} = \frac{120\%}{\sqrt{E(GeV)}} \oplus 6.9\%. \tag{3.7}$$

3.2.6 Superconducting Magnet

The large solenoidal magnet, with a bore measuring 5.9 m in diameter and 12.9 m in length, is one of the detectors central components. The magnetic flux density (B) within the bore is 3.8 T. The strength of B is one of the factors that determines the transverse momentum resolution (Δp_T) and the charge misidentification rate of high

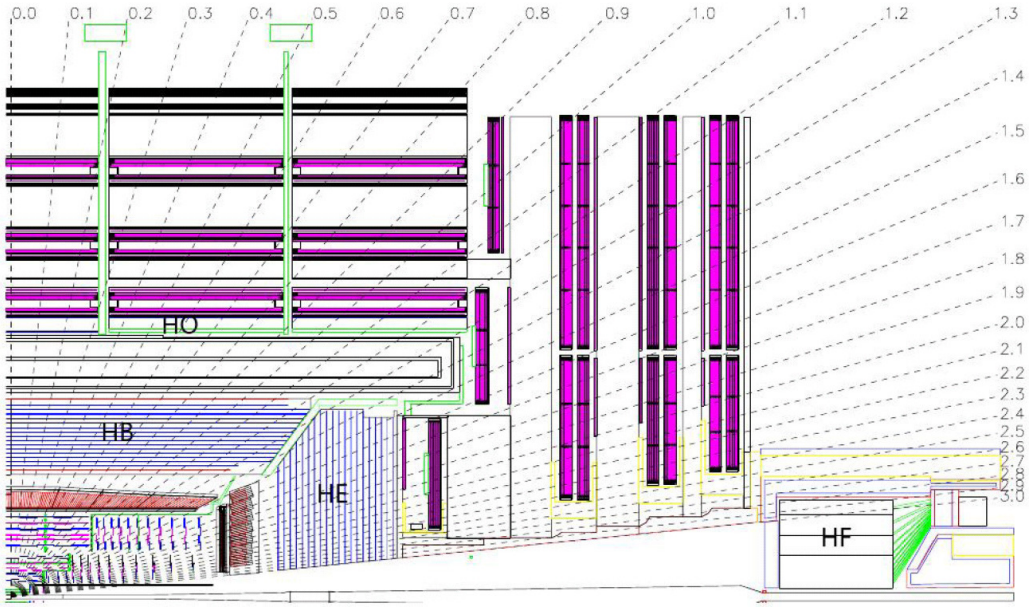

Figure 3.5: Schematic view of the hadronic calorimeter and other sub-detectors of CMS. Dashed lines indicate η.

energetic particle tracks. Both quantities, p_T and the charge q, are measured via the radius of curvature R of the $x - y$ projection of a particle track since

$$R \approx \frac{p_T}{qB}. \tag{3.8}$$

The design goal of CMS was to achieve a relative momentum resolution of 10% for muons with momentum of 1 TeV. In order to reach such a high magnetic flux, it is necessary to use a superconducting coil, operating at a temperature of 4.6 K.

3.2.7 Muon System

To identify muons and measure their momenta, CMS uses three types of gaseous detectors. The detectors are interspersed with layers of the magnet return yoke. This setup serves both as a hadron absorber and a second handle on measuring the muon

momentum. The muon system comprises a cylindrical barrel region and two endcaps, similar to other CMS sub-detectors. A transverse view of the CMS barrel muon detector can be seen in Figure 3.6. In the barrel region, drift tube (DT) chambers are used, with separate cells to allow for position measurements in the $r\phi$-plane and z-direction. The cells overlap to prevent dead spots. The geometry was selected to provide maximal efficiency for reconstructing individual muon trajectories and rejecting background hits. The cathode strip chambers (CSC) are utilized in the endcaps where the magnetic field is non-uniform and particle rates are high. The CSC provides a fast response time, fine segmentation, and resistance to radiation. A dedicated system for triggering was also installed, making use of resistive plate chambers (RPC) in both the barrel and endcaps. These devices are independent from the DT and CSC. They provide a fast response, but coarser position measurement. Combined with the DT and CSC, they help to resolve ambiguity in constructing muon tracks from potential multiple hits in a chamber.

3.2.8 Trigger and Data Acquisition

The nominal LHC design luminosity of 10^{34} $\mathrm{cm}^{-2}\mathrm{s}^{-1}$ results in an expected proton-proton interaction rate of order 10^3 MHz. The actual event rate during the 2011 and 2012 runs was reduced to 20 MHz. Online data selection is an extremely difficult task and determines the overall performance of the experiment. The average size of an event is approximately 1 MB and the maximum bandwidth for storing data on disk or tape is in the order of 100 MB/s. Thus the trigger system of CMS has been designed to reduce an event rate of 40 MHz up to an order of 100 Hz. In CMS this task is split into two steps.

The first step is the L1 trigger. It is implemented using custom-designed elec-

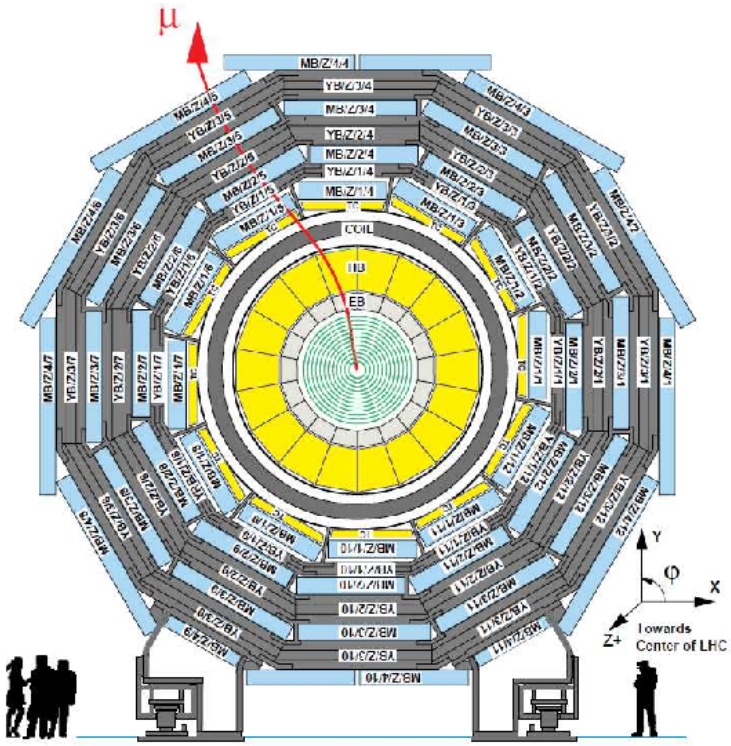

Figure 3.6: Transverse view of the CMS barrel muon detector. A typical muon track is also shown (red curve).

tronics, such as FPGA's, ASIC's and programmable memory lookup tables (LUT), which allow flexibility but also fulfill speed requirements. The L1 trigger is designed to achieve a rate reduction of the order of 10^3, resulting in a maximal output rate of 100 kHz. The schematic overview of the L1 trigger system is shown in Figure 3.7. It uses coarse segmented data from the muon system and from the calorimeters, while the complete raw data is pipelined in the front-end electronics until being rejected or accepted for further processing by the High-Level Trigger (HLT). The allowed latency between the bunch-crossing and the L1 Trigger decision is 3.2 μs. The calorimetric trigger branch combines signals from the ECAL and the HCAL to provide information about jet related quantities like multiplicities, individual energies or their total

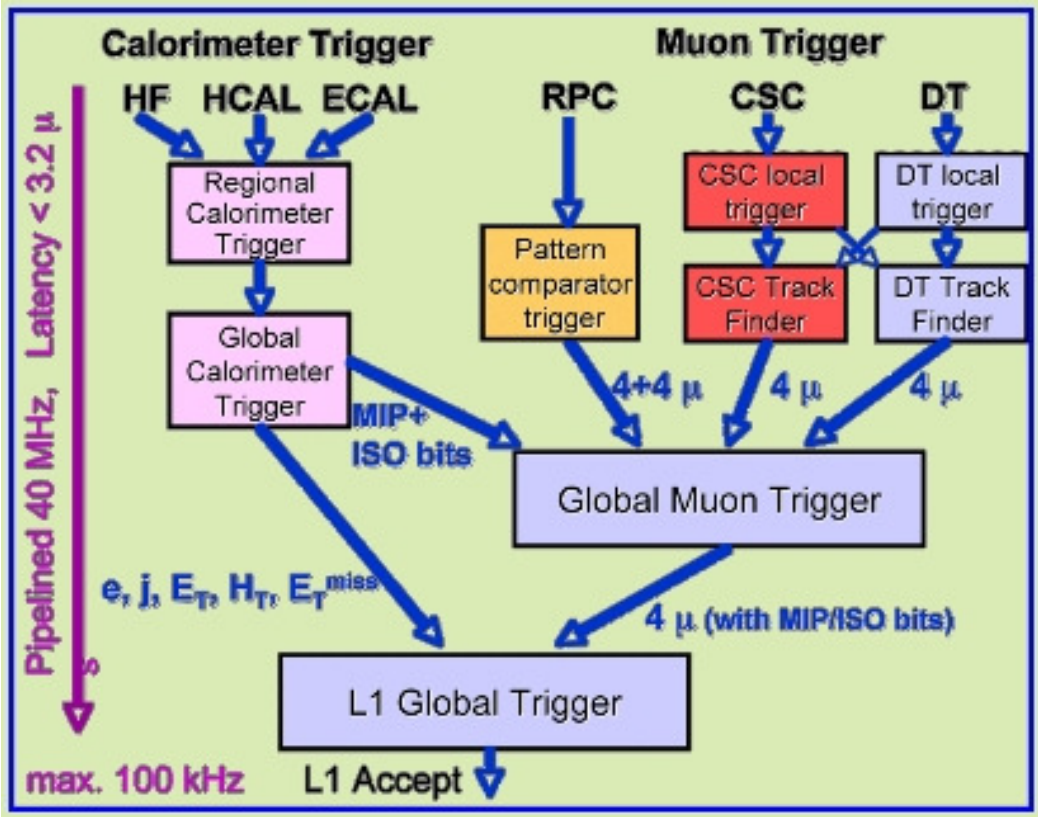

Figure 3.7: Architecture of the Level-1 Trigger system.

energy, as well as the missing transverse energy of the event. It can pass information about the energy deposit in the vicinity of muons to the muonic trigger branch. The muonic branch combines information of all three muon systems, namely, the DT's, the CSC's and the RPC's. It delivers up to four final muon candidates, sorted by their transverse momentum to the Global Trigger (GT). The GT calculates the final L1 trigger decision based on information from both branches. Up to 128 programmable algorithms can be executed in parallel. Additionally 64 so called technical triggers can be considered based on direct signals from the subdetectors.

After being accepted by the L1 trigger, the full event data stored in the various front-end buffers of the subdetectors are collected by the data acquisition (DAQ) sys-

tem. At this point, the DAQ has to handle a data flow of about 100 GB per second, which is distributed to the software based filter system of the HLT [39]. The HLT runs on a computer farm and uses fast versions of the same algorithms that are run in the offline event reconstruction. The main strategy to speed up the event processing is to reject unwanted events as early as possible. Typically, the reconstruction starts with information from the calorimeters and the muon detectors before tracker information is added. Because of the high number of channels and the complex pattern recognition, the full reconstruction of trajectories in the tracker is expensive in CPU time. Therefore, a partial reconstruction, involving only information from the pixel detector, is used for trigger decisions.

Chapter 4

Datasets and Triggers

4.1 Integrated Luminosity

The instantaneous luminosity measurement gives the average number of collisions per bunch crossing. Integrating this quantity over the total time that the detector is in operation, gives the total data delivered which is called the integrated luminosity. The total proton-proton collision data that the LHC delivered in 2012 is around $\mathcal{L} = 23.3\ fb^{-1}$. Measurement of the instantaneous luminosity is conducted whenever the LHC is operational, whether or not CMS is taking data. Therefore, the integrated luminosity delivered by the LHC machine and the total luminosity recorded by CMS are slightly different. CMS recorded 94% of the data delivered by the LHC in 2012, totalling 21.79 ± 0.48 fb^{-1}. The integrated luminosity is measured to 2.2% accuracy. The delivered and recorded luminosities as a function of time can be seen in Figure 4.1.

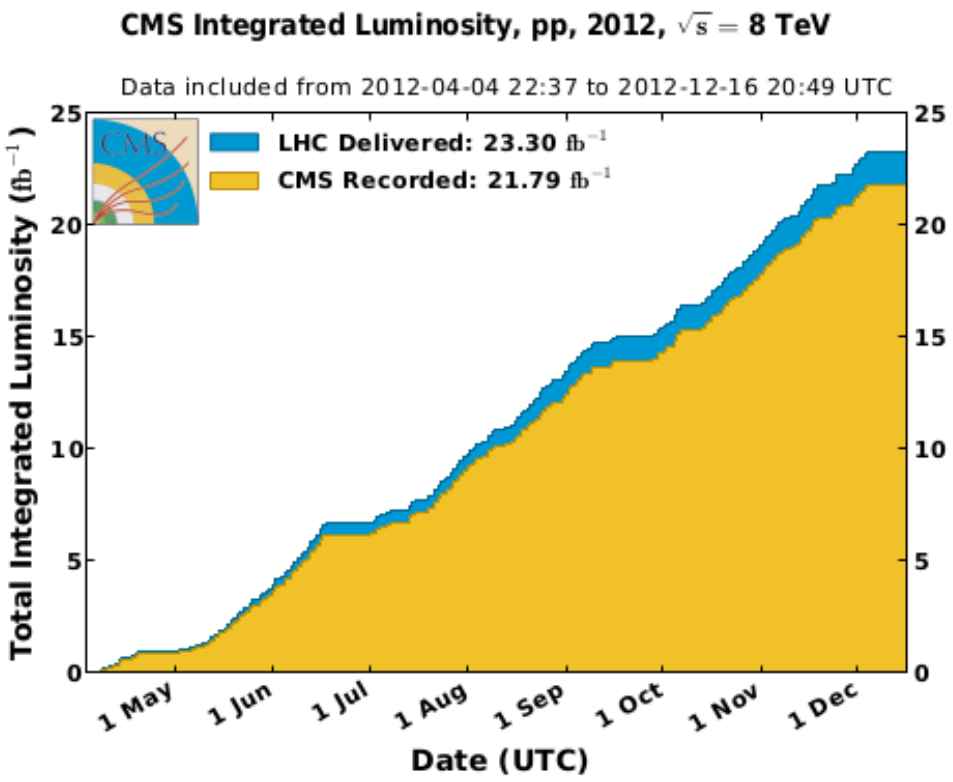

Figure 4.1: Cumulative luminosity delivered to (blue) and recorded by CMS (orange) during stable beams for proton-proton collisions at $\sqrt{s} = 8$ TeV in 2012.

4.2 Data Certification

There is no quality selection imposed when the data is reconstructed in CMS. Instead, the data which is tagged as good by all physics object groups (POG's) and subdetectors are collated into a JavaScript Object Notation (JSON) file. This file contains all run ranges and the corresponding luminosity sections of good quality data. Around 90% of the 21.79 fb^{-1} recorded by CMS in 2012 is certified as good for all analyses. This represents an integrated luminosity $\mathcal{L} = 19.6$ fb^{-1} at $\sqrt{s} = 8$ TeV. The JSON file used for this analysis is Cert_190456-208686_8TeV_22Jan2013ReReco_Collisions12_JSON.txt which corresponds to run ranges from 190,456 to 208,686.

Table 4.1: Primary dataset used in the analysis.

Dataset
/PhotonHad/Run2012A-22Jan2013-v1/AOD
/PhotonHad/Run2012B-22Jan2013-v1/AOD
/PhotonHad/Run2012C-22Jan2013-v1/AOD
/PhotonHad/Run2012D-22Jan2013-v1/AOD

Table 4.2: HLT triggers used in the analysis.

Trigger Name
HLT_Photon70_CaloIdXL_PFHT400
HLT_Photon70_CaloIdXL_PFNoPUHT400

4.3 Dataset

The full data stream recorded by CMS is split into several primary datasets in order to reduce the amount of data over which a particular physics analysis needs to run. HLT paths, also called HLT triggers, which require similar physics objects, are grouped into datasets. The PhotonHad datasets are used in this analysis as listed in Table 4.1. These datasets represent $\mathcal{L} = 19.5$ fb^{-1} at $\sqrt{s} = 8$ TeV.

A trigger menu that requires the simultaneous presence of a single photon with transverse momentum, p_T, greater than 70 GeV and hadronic transverse energy, H_T, greater than 400 GeV is used. The hadronic transverse energy is the scalar sum of the p_T of the selected jets in an event. Particularly, for the first 5.3 fb^{-1} of 2012 data the HLT_Photon70_CaloIdXL_PFHT400 trigger is used. Then the trigger was updated to HLT_Photon70_CaloIdXL_PFNoPUHT400 for the remaining 14.3 fb^{-1} data. In the updated trigger, the jets used for the H_T calculation are corrected for pileup. The triggers and the terminology used in the trigger names are summarized in Table 4.2 and Table 4.3, respectively.

Table 4.3: Trigger Cuts.

Dataset	Requirements
Photon70	Photon supercluster P_T >70 GeV
CaloIdXL	$H/E < 0.10$, $\sigma_{i\eta i\eta} < 0.014$
PFHT400	Sum of particle flow jets $P_T > 400$ GeV*
PFNoHT400	PFHT400 using pileup-corrected P_T

* Only jets with P_T >40 GeV and $|\eta| < 3.0$ are considered.

4.4 Trigger Efficiency

The efficiency of the triggers used in this analysis is measured separately for the photon p_T and the H_T leg, using the tag-and-probe method [40] with two different baseline triggers.[1] A pure H_T trigger, HLT_PFNoPUHT650, was used as baseline for computing the efficiency of the HLT_Photon70_CaloIdXL leg. On the other hand, a single photon trigger, HLT_Photon150, was used as baseline to determine the efficiency of the HLT_PFNoPUHT400 leg.

Figures 4.2 and 4.3 shows that both the H_T and the photon p_T trigger legs have a constant efficiency over the phase space considered in the analysis. The red vertical dashed lines in the plots indicate the cut where the trigger becomes fully efficient.

[1]Trigger effeciency figures and results were produced by Valentina Sola.

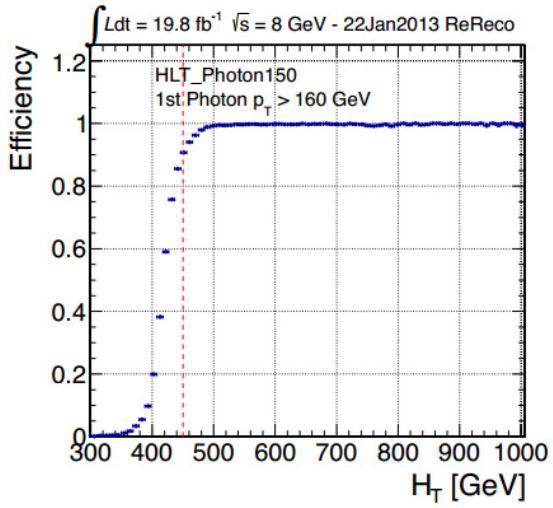

Figure 4.2: Trigger efficiency of the H_T leg for the HLT triggers used in this analysis. The corresponding base-line triggers and cut values used are labelled on the plot. The red vertical line indicates the H_T value where the H_T leg of the trigger becomes approximately fully efficient.

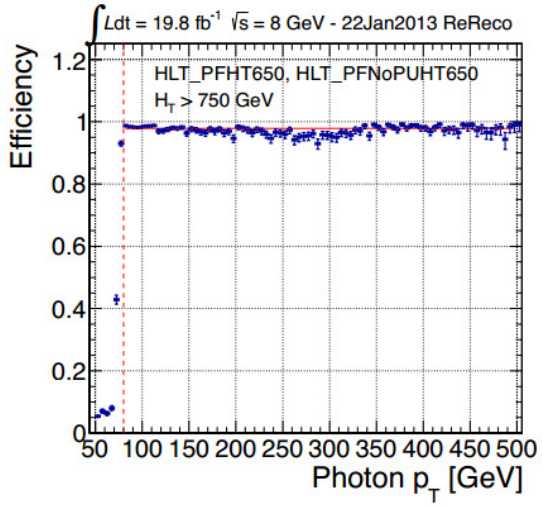

Figure 4.3: Trigger efficiency of the p_T leg for the HLT triggers used in this analysis. The corresponding base-line triggers and cut values used are labelled on the plot. The red vertical line indicates the p_T value where the p_T leg of the trigger becomes approximately fully efficient.

Chapter 5

Physics Object Reconstruction and Identification

The data collected by the CMS detector with the L1 trigger are electronic signals. These signals contain amplitude, timing and position information which needs to be converted into physical quantities, e.g. momentum, energy, or track coordinates. From this information, physical objects (e.g. photons, electrons, jets, etc.) will be reconstructed which form the basis of a data analysis. This chapter describes how event objects are reconstructed.

5.1 Beam Spot and Vertex

When two proton bunches cross, some protons in one bunch interact with some protons in the opposite bunch. Each hard collision between a parton in one proton and another parton in the other interacting proton produces several particles originating from the point of collision. This point is referred to as the primary interaction vertex. Since proton bunches have a finite size, the interaction point of proton-proton colli-

sions do not always occur at exactly the same point. Instead, they are distributed over a finite region. This small volume of collision points is called the beam spot. The short-lived particles originating from the initial collision can decay at some distance away from the primary interaction point and then decay to multiple secondary particles. This point is referred to as the secondary vertex. After the beamspot is determined, the primary vertices are reconstructed. The task of reconstructing primary vertices consists of vertex finding and vertex fitting. The primary vertices are found by sorting all tracks in the event into sets with a common origin. First the tracks having a small impact parameter with respect to the beam-line are selected. Then the selected tracks are grouped together based on the z-axis of the track's intersection with the beam-line. The selected tracks are then clustered along the z-axis by requiring a separation of at least 1 cm to the next cluster. Then, a vertex candidate for each group of tracks is determined by using an adaptive vertex fitter [41]. The fitter assigns each track a weight,

$$w_i = \frac{\exp(-\chi_i^2/2T)}{\exp(-\chi_i^2/2T) + \exp(-\sigma_{cut}^2/2T)} \ ,$$

with $\chi_i^2 = d_i^2/\sigma_{d_i}^2$, where d_i and σ_{d_i} are the track's distance to the vertex and its error, σ_{cut}^2 defines the cut on the track's χ_i^2, and T defines the softness of this cut. The value of T is chosen by trial and error. T equal to zero corresponds to the hardest cut. Each fitted vertex is then assigned a number of degrees of freedom, which is defined as:

$$n_{dof} = 2 \sum_{i=1}^{nTracks} w_i - 3. \tag{5.1}$$

5.2 Track Reconstruction

Determining the trajectory of a charged particle in the magnetic field allows the deduction of the kinematic properties of that particle. This trajectory is a helix with an axis along the magnetic field. The trajectory is described by five parameters: the radius of curvature R, the perpendicular and longitudinal distance of the closest approach of the helix to the beam spot $d_{xy}(bs)$ and $d_z(bs)$, respectively, and the angles ϕ and θ, that the track forms at the point of closest approach (PCA) with the x-axis in the plane perpendicular to the magnetic field and with the z-axis in the plane parallel to the magnetic field. The track parameters are illustrated in Figure 5.1.

By knowing the parameters of the particle's trajectory at various points in the detector, the location of the particle's origin, its momentum, the sign of its charge,

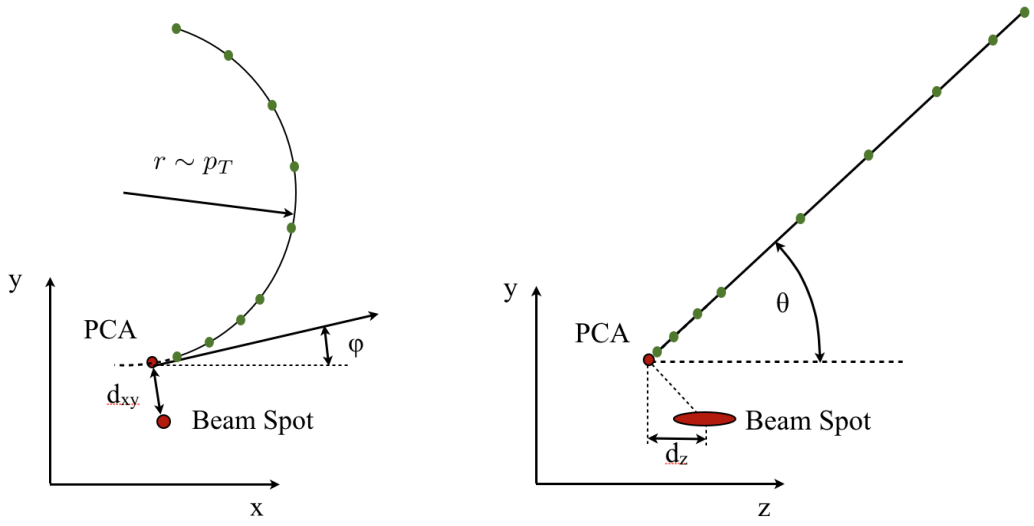

Figure 5.1: Schematic views of a particle's trajectory in the $r-\phi$ plane (left) and the in $r-z$ plane (right) showing the five track parameters. In the $r-\phi$ plane: the radius of the trajectory which is proportional to the transverse momentum of the particle, $r \sim p_T$, the 2D distance from the beam spot to the point-of-closest-approach (PCA), $d_{xy}(bs) = (x_{PCA} - x_{BS})\sin\phi - (y_{PCA} - y_{BS})\cos\phi$, and the azimuthal angle of the trajectory at the PCA ϕ. In the $r-z$ plane: the z-coordinate of the PCA with respect to the beam spot $d_z(bs) = z - z_{BS}$ and the polar angle θ at the PCA, in the track reconstruction $\cot\theta = \frac{p_z}{p_T}$ is commonly used. The magnetic field is along z.

and how much energy it has lost while traversing the detector can be determined. As a charged particle traverses the detector, it leaves a trace of small energy deposits in each tracker sensor that it crosses. The positions of these energy deposits are used to find the parameters of the particle trajectory and then reconstruct the trajectory itself. This is done by the track reconstruction software. The track reconstruction in CMS is performed in six iterations [42–44]. Each iteration starts with a different set of seeds, which are trajectories defined by a minimum of three points, and then proceeds using the same algorithm for each iteration. Each iteration consists of five steps that are described below.

First, in each sensor the clusters are formed out of contiguous sets of strips or pixels with a signal above threshold. Then, the signal distribution between the pixels or the strips in a cluster is analysed, using templates developed during test beam experiments, and the hits are formed. The hits carry information about the position and the error on the position. In the second step, trajectory seeds are generated using a minimum of three tracker hits with their associated three-dimensional position measurements. The seeds for each iteration are constructed differently. Overall, four types of seeds are used. Since more than 90% of the charged particles produced in the proton-proton collisions will cross three pixel layers, the seeding for many iterations starts in the pixel detector. Pixel triplets give the most precise estimation of the trajectory parameters, hence they are used first. In order to find them, a loose beam spot constraint is used to filter out trajectories that did not originate from the interaction region. However, once the seed is constructed the beam spot position is not use to estimate the initial trajectory parameters. Another type of seeds are pixel and strip pairs with vertex constraint. They use vertices reconstructed using tracks from the previous iteration. The vertex constraint is used to build the trajectory but is removed before determining the final trajectory parameters. The third type of

Iteration	Seeding Layers	p_T	d_{xy}	d_z	Constraint
		GeV	cm	cm	
0	pixel triplets	0.5	0.2	15.9	beam-spot
1	pixel/strip pairs	0.9	0.2	0.2	vertex
2	pixel triplets	0.075	0.2	17.5	beam-spot
3	pixel/strip pairs	0.35	1.2	7.0	beam-spot
4	strip pairs	0.5	2.0	10.0	beam-spot
5	strip pairs	0.8	5.0	10.0	beam-spot

Table 5.1: The parameters used to build seed-trajectories for each iteration. The d_z and d_{xy} were calculated with respect to the CMS center. Both d_z and d_{xy} are calculated with respect to the interaction vertex.

seeds are pixel and strip pairs with beam spot constraint. Although it is similar to the previous type, the looser beam spot constraint helps to recover the decays of long-lived hadrons, such as pions and kaons. The fourth type of seeds are the strip-only pairs with beam-spot constraint, which use three-dimensional strip measurements to construct seeds for trajectories which may not have had any pixel hits. As before, the beam spot constraint is removed before determining the final trajectory parameters. The seeds for each iteration are summarized in Table 5.1.

In the third step, the trajectories are built using a Combinatorial Track Finder (CTF) algorithm [45] which is based on the Kalman filter method [46]. In the application to track finding, the Kalman filter uses not only the weighted average of the previous measurements of the trajectory but also the law of motion of the charged particle in the magnetic field in order to predict the next trajectory measurement.

Starting from a seed, the CTF builds the particle trajectory one hit at a time. A hit is added if the χ^2 of the trajectory calculated including this hit is smaller then a predetermined value. If several hits pass this requirement, then several new trajectories are created. In addition, a trajectory with no hit in a layer is also created to account for the possibility of detector inefficiency. This absent hit is called an

"invalid" hit. However, the trajectory is not allowed to have two "invalid" hits in a row at the building stage.

The track finding algorithm can result in several trajectories from the same seed. Since multiple trajectories are built simultaneously, several trajectories originating from different seeds may merge. These ambiguities are resolved in the fourth step. The number of shared hits between two trajectories is examined:

$$f_{shared} = \frac{N_{shared}}{\min(N_1^{hits}, N_2^{hits})}.$$

If f_{shared} is more than 50%, then the trajectory with the fewest hits is discarded. If both trajectories have the same amount of hits then the trajectory with the higher χ^2 value is discarded. Finally, the trajectories are re-fitted a final time using again the Kalman filter method. The residual errors of each hit are re-evaluated after the final fit and the hits with a residual error larger than a pre-determined value are discarded and replaced by "invalid" hits. After a hit has been discarded, the track is re-fitted again and new hit residual errors are calculated. This procedure is repeated until the residual errors of all hits are smaller then a pre-determined threshold.

The general track collection are the tracks in the central tracker reconstructed with the CTF algorithm. This collection does not include the stand-alone tracks reconstructed in the muon detectors, the global muon tracks with hits in both the tracker and the muon detectors and the electron tracks reconstructed by the Gaussian sum filter algorithm. It does include electron tracks that are reconstructed with the CTF algorithm.

5.3 Electron

To reconstruct electrons, CMS uses two complementary approaches. One method is ECAL-driven while the other one is tracker-driven. The ECAL-driven reconstruction [47] builds clusters from energy deposits in the electromagnetic calorimeter within a narrow η range, which extends over a wide range in the azimuthal direction, ϕ, in order to catch bremsstrahlung radiated by the electron when traversing the tracker material. While traversing the ECAL, an electron encounters a large amount of material and loses energy by emitting bremsstrahlung photons as seen in Figure 5.2. Although the electron travels along a curved trajectory, the radiated photons travel in a straight line on a tangent to the electron trajectory.

Thus the pattern of energy deposits in the calorimeter is a narrow trail of clusters in the ϕ-direction, left by each radiated photon along with the electron itself. In order to calculate the total energy of the electron, these clusters are combined into one super-cluster. The reconstruction of the electron super-cluster is done first by

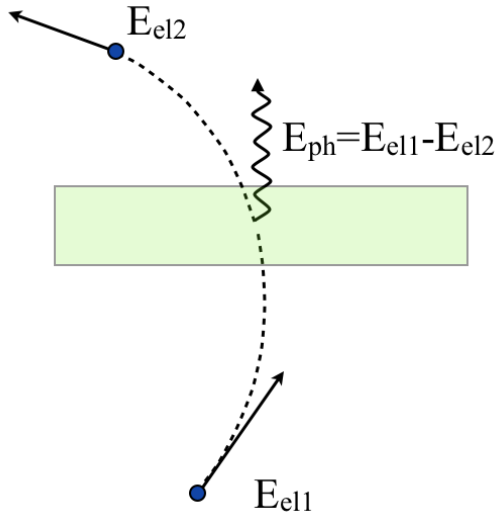

Figure 5.2: Electron with energy E_{el1} traversing a material emits a bremsstrahlung photon loosing energy, $E_{el2} = E_{el1} - E_{ph}$, in the process.

combining individual calorimeter towers with energy above threshold into clusters, and then combining all clusters along a narrow strip in ϕ into the super-cluster, see Figure 5.3.

Electron tracks are then reconstructed starting from matched seeds using a Gaussian Sum Filter (GSF) [49], which is able to cope with energy loss due to bremsstrahlung.

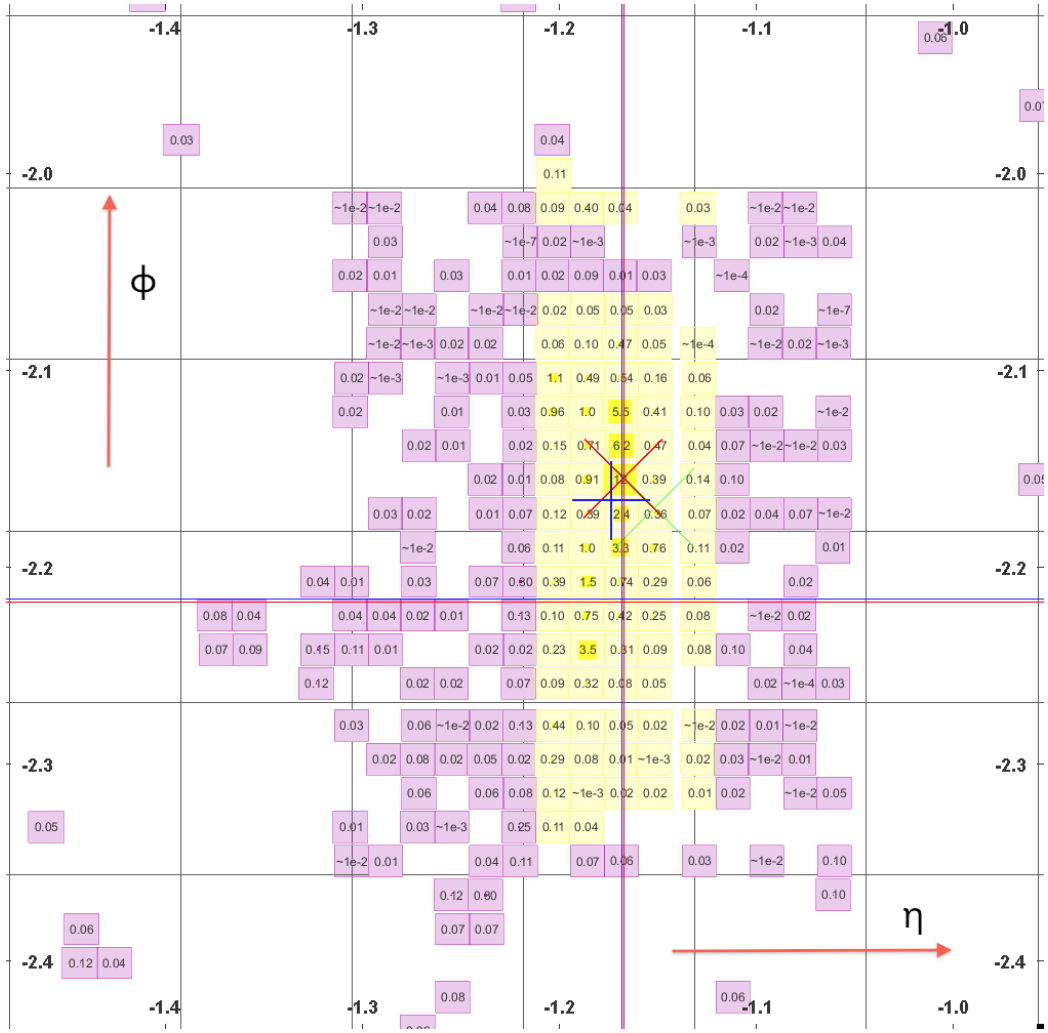

Figure 5.3: Electromagnetic calorimeter towers grouped into electron supercluster (yellow). The pink squares are unclustered towers. Blue cross + indicates supercluster centroid. Green × indicates direction of the electron at vertex. Red × indicates seed cluster centroid. The azimuthal angle ϕ is along the vertical axis and pseudo-rapidity η is along the horizontal axis. The image is produced in CMS visualization software cmsShow [48].

This approach is well-suited for isolated high momentum electrons.

The ECAL-driven approach is complemented by the tracker-driven reconstruction, which is able to reconstruct low momentum electrons starting from 2 GeV. Its efficiency is less dependent on the electron isolation. Since the GSF fit is CPU intensive, all tracks that are reconstructed by the fast Kalman filter are tested for their compatibility with the electron hypothesis, based on track quality criteria. The track quality is typically worse for electrons, because energetic bremsstrahlung emission cannot be handled by the Kalman filter. Compatible tracks are then used as seeds for the GSF fit, which is extrapolated to the ECAL to find the energy deposit of the electron. Energy deposits from bremsstrahlung are associated to the electron candidate by extrapolating a tangent to the electron track at each tracker layer to the ECAL.

The following variables are used to identify electrons and to differentiate prompt electrons from misidentified or non-prompt electrons:

- H/E: The ratio of energy deposits in the HCAL and the ECAL.

- $|\Delta\eta_{in}| = |\eta_{sc} - \eta_{in}^{extrap.}|$ and $|\Delta\phi_{in}| = |\phi_{sc} - \phi_{in}^{extrap.}|$: the distance between the position of the GSF track extrapolated from the innermost measurement of the track to the innermost surface of the electromagnetic calorimeter, $(\eta_{in}^{extrap.}, \phi_{in}^{extrap.})$, and the center-of-mass of the super-cluster (η_{sc}, ϕ_{sc}).

- $\sigma_{i\eta i\eta}$: The square of the energy weighted width in pseudo-rapidity of the super-cluster.

- Number of missing inner tracker hits.

- $|d_{xy}|$ and $|d_z|$: Impact parameter with respect to the primary vertex.

- Combined relative isolation: the sum of all the isolation deposits (described below) divided by the value of the transverse momentum of the electron.

In the tracker, the scalar sum of the transverse momentum of all tracks with transverse momentum $p_T > 0.7$ GeV, distance to the vertex of $d_{xy}(pv) < 0.2$ cm, and within a hollow cone $0.04 < \Delta R < 0.3$ is calculated. The isolation deposits in the electromagnetic calorimeter are calculated by summing up all transverse energy in a hollow cone with outer radius $\Delta R < 0.3$ and inner cone radius of three calorimeter crystals ($\Delta R \approx 0.05$ in the barrel). In order to exclude energy from bremsstrahlung photons, the deposits from a narrow strip along the azimuthal direction with a width in η of three calorimeter crystals are excluded. Also, to exclude noise a threshold of $E = 0.08$ GeV in the barrel and $E_T = 0.1$ GeV in the end-cap was applied to all crystals used in the calculation of isolation deposits. The isolation deposits in the hadronic calorimeter were simply calculated by summing up all hadronic calorimeter towers with energy above 0.7 GeV in the barrel and above 0.8 GeV in the end-cap using a hollow cone with outer radius of 0.30 and a veto cone radius of 0.15.

5.4 Photon

Photon clustering begins with energy deposits in an ECAL crystal. A crystal with the highest energy deposit compared to its neighbors is labeled the seed crystal. A region of crystals surrounding this seed crystal corresponding to 3 crystals in η by 3 crystals in ϕ (3×3) is defined and a larger region corresponding to an area of 5×5 crystals. If the ratio $r9 = E_{3\times3}/E_{5\times5} > 0.93$, the photon is tightly clustered and is unlikely to have converted to an e^+e^- pair. It is thus labelled as unconverted and the 5×5 region is assigned as the photon supercluster energy. If the ratio is less than 0.93, the photon is assumed to be a conversion, and the super-clustering is

performed by starting with the seed crystal and working outward radially, keeping crystals which have deposits above a nominal threshold and a lower energy than the previously added crystal, and rejecting crystals which have no energy readout or show an increase in energy deposit. This avoids adding detector noise to the energy calculation and avoids double counting of energy deposits over multiple photons.

An important variable used to discriminate photons and electrons from π^0 contamination is the "width" in η of the electromagnetic shower $\sigma_{i\eta i\eta}$, given by the following expression:

$$\sigma_{i\eta i\eta} = \sqrt{\frac{\Sigma_i^{5\times5}\left(0.01745\eta_i + \eta_{seed\,crystal} - \langle\eta\rangle_{5\times5}\right) w_i}{\Sigma_i^{5\times5} w_i}} \tag{5.2}$$

where w_i =max$\left(0, 4.2 + \ln\left[\frac{E_i}{E_{5\times5}}\right]\right)$.

A common selection criteria in photon identification is to limit the hadronic deposit that comes from the candidate photon. The variable H/E is defined as the ratio of the energy measured by the HCAL tower directly behind the ECAL seed crystal divided by the photon supercluster energy. Ensuring that this ratio is small increases the photon selection purity and improves the photon energy resolution in the case where the photon exits the ECAL without depositing all of its energy.

A powerful variable in photon identification is the isolation of the photon object. Isolations make use of the particle flow (PF) algorithm described in Section 5.6. Factors in the isolation include contributions from three sources: charged hadrons (chargedHadronIso), neutral hadrons (neutralHadronIso) and electromagnetic objects (photonIso). The isolation itself is calculated as the E_T of the contributing objects in a cone of $\Delta R = \sqrt{(\phi_{track} - \phi_{photon})^2 + (\eta_{track} - \eta_{photon})^2} = 0.3$ centered around the photon seed.

As described in Section 3.2.2, the pixel detector is used in measuring the track

parameters of a particle that pass through it. The minimum requirement for a pixel seed is two hits in different layers of the pixel detector in order to match an electromagnetic deposit in the ECAL and the interaction vertex. Requiring no pixel hits minimizes the misidentification of electrons as photons.

5.5 Muon

Due to the nature of the CMS detector, identification of muons is more efficient and misidentification contamination is much less than for electrons. Muons are much heavier than electrons and therefore their energy loss in material is much less. Thus they leave only a track in the central tracker system, a small energy deposit in the calorimeters, and penetrate the calorimeters, the solenoid, and the return yoke steel leaving a track in the muon system.

The reconstruction of muons uses both the tracker and the muon systems. From the muon systems, standalone-muon tracks are reconstructed independent from the silicon tracks [50]. Standalone-muon tracks are also reconstructed using the Combinatorial Track Finder described in Section 5.2. Using both the silicon tracks (tracker tracks) and standalone-muon tracks, the following muon reconstructions are produced:

- Global muon: The stand-alone muons tracks and the tracker tracks are matched. For each stand-alone muon track a group of the tracker tracks is chosen based on the spatial variables and momentum difference. Then, all the pre-selected tracker tracks are propagated out to a common surface between the central tracker and the muon chambers. The stand-alone muon tracks are also propagated into the same surface. The parameters of the trajectories of the tracker tracks and of the stand-alone muon track on that surface are then compared

to find the best match. Finally, a global fit is performed using hits in the tracker track and the stand-alone muon track. This method can improve the momentum resolution for high-transverse momentum muons ($p_T > 200$ GeV) as compared to using only the tracker track.

- Tracker muon: All tracker tracks with $p_T > 0.5$ GeV and $p > 2.5$ GeV are assumed to be potential muon candidates. These tracks are extrapolated up to the muon system. When the extrapolated track matches at least one muon segment, this track will be regarded as a tracker muon.

- Standalone muon: All standalone-muon tracks that are not matched to a tracker track are classified as a standalone muon. Most of these muons are from cosmic rays. Only about 1% of the standalone muons come from pp collisions [51].

5.6 Particle Flow Algorithm

The particle flow algorithm [52] attempts to reconstruct all stable, strongly or electromagnetically interacting, particles in the event, that is, electrons, photons, muons, and all charged and neutral hadrons, using information from all of the CMS subdetectors. The resulting particles are then used to reconstruct higher level observables, such as jets, missing transverse energy, etc. In this analysis we use the particle flow framework to reconstruct jets and missing transverse energy.

5.6.1 Particle Flow Jet

The process of hadronization (formation of hadrons from quarks and gluons) results in a number of hadrons in a tight cone around the original quark or gluon direction. These cones of hadrons are called jets.

In the particle flow framework, jets are defined as groups of any reconstructed particles that have been grouped according to some jet clustering algorithm. In this analysis, the anti-k$_T$ jet clustering algorithm [53] is used. One great feature of the anti-k$_T$ algorithm, aside from being computationally fast, is that soft particles do not modify the shape of the jet. It is also robust even in cases where the energy of a jet is distributed between two collinear particles. The criteria for clustering particles into a jet are the following:

$$d_{ij} = \min(k_{ti}^{2p}\ ,\ k_{tj}^{2p})\frac{\Delta_{ij}^2}{R^2} \tag{5.3}$$

$$d_i = k_{ti}^{2p} \tag{5.4}$$

where $\Delta_{ij}^2 = (\eta_i - \eta_j)^2 + (\phi_i - \phi_j)^2$ with k_{ti}, η_i, and ϕ_i are the transverse momentum, pseudo-rapidity, and azimuthal angle of the particle i, respectively, and R is the radius that defines the jet. The algorithm loops over all entities (particles, clusters of particles) and compares the smallest d_{ij} and d_i. If d_{ij} is smaller, then the i and j entities are clustered, if d_i is smaller, then it is called a jet and removed from the list. The traditional k_t algorithm uses $p = 1$, thus for the anti-k_t algorithm $p = -1$. It is easy to demonstrate that with the anti-k_t condition the clustering algorithm prefers to cluster around hard particles, thus forming nice conical jets with a hard particle center, while the jets of the soft particles in the neighborhood of the hard particles will have deformed cones as can be seen in Figure 5.4.

The anti-k_t jet clustering algorithm with the jet cone size $R = 0.5$ is the default jet clustering algorithm in CMS. Thus it is used in this analysis within the particle flow framework. Except for applying a threshold on the jet transverse momentum and assuring that a jet was not coinciding with one of the selected leptons, no additional jet identification variables were used in this analysis.

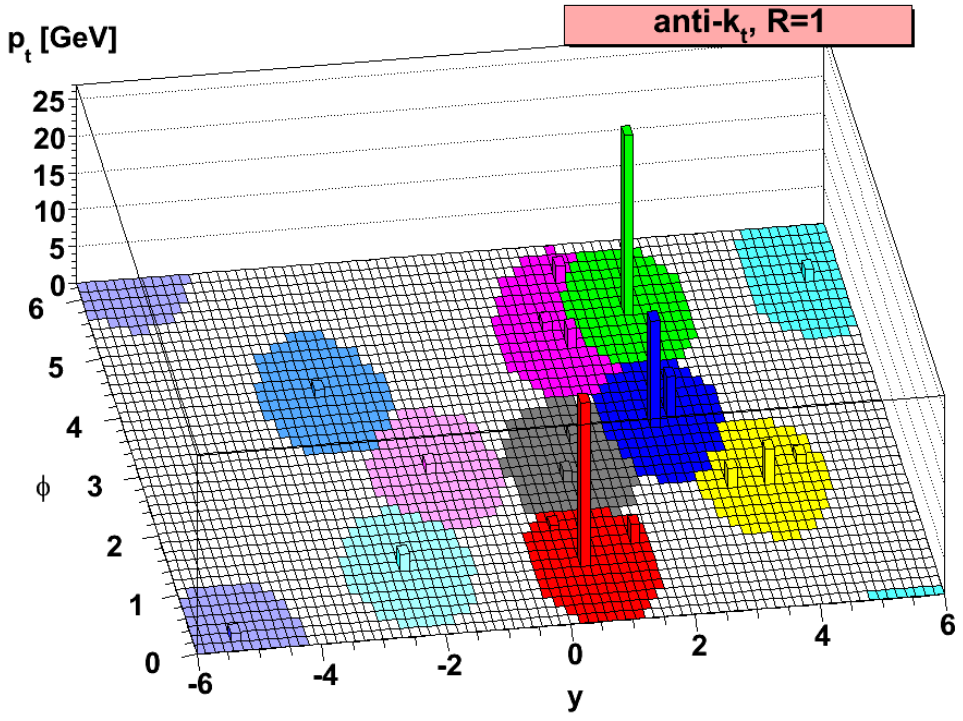

Figure 5.4: Example of the anti-k_t jet clustering algorithm at work. The cones around the hard particles are nice and round, while the cones of the soft particles, in close proximity to the cones of the hard particles, are deformed. For more detail see Reference [53].

5.6.2 Missing Energy

The initial colliding protons in the LHC have negligible transverse momenta. Momentum conservation thus implies that the sum of all final-state particle transverse momenta should be close to zero, unless there are weakly interacting particles (e.g. neutrinos) in the final state that are not reconstructed. The transverse momentum imbalance is refered to as the missing transverse energy, E_T^{miss}.

In CMS three different techniques are employed in reconstructing E_T^{miss}: calorimeter E_T^{miss} (caloMET), track-corrected E_T^{miss} (tcMET) and particle-flow E_T^{miss} (PFMET). The caloMET is a traditional method which uses only calorimeter information in reconstructing E_T^{miss}. The track-corrected tcMET is similar to caloMET but with a better hadronic energy correction. Finally, the particle-flow E_T^{miss} is measured using all the particles reconstructed in the detector. Therefore it gives the best resolution and is consequently used in this analysis.

Since the particle flow algorithm reconstructs all particles, the calculation of the missing transverse energy proceeds in a straightforward fashion. It is expressed as

$$E_T^{miss} = \left| -\sum_i \vec{p}_{T,i} \right|$$

where i runs over all particle-flow particles in an event.

Chapter 6

Analysis Strategy and Event Selection

6.1 Analysis Strategy

As discussed in Chapter 2, the framework being considered in this study is supersymmetry based on the MSSM with GMSB and a wino-like NLSP together with R-parity conservation. This scenario results in an event topology containing large E_T^{miss}, multiple jets, a lepton, and a photon. For this analysis, we only consider electrons (see Figure 6.1). From the figure we can also see a lot of jet activity resulting in high H_T, which is the reason behind the HLT path choosen in this study. The event selection will be detailed in the next section.

The event scenario being considered could also be mimicked by standard model processes, which will appear as background in this analysis. This is the reason why it is important to model SM backgrounds well. The analysis backgrounds will be discussed in Chapter 7.

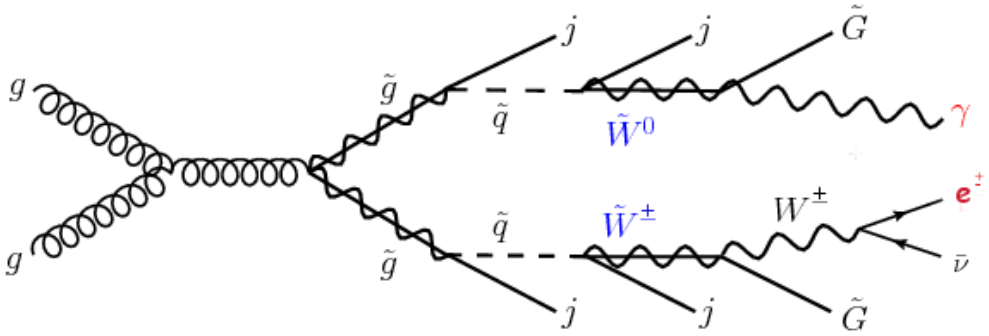

Figure 6.1: Feynman diagram of a GMSB wino-like neutralino process.

6.2 Event Selection

Basic event cleaning has been applied on all data samples to reduce the effects of known sources of noise and preselect good collision events. Most of the cleaning is applied by default in the CMS reconstruction software (CMSSW). The HLT requirement is then applied, and the following criteria are required for the signal or simulated sample events:

- a good quality vertex,
- hadronic transverse energy, H_T, greater than 450 GeV,
- at least one tight electron with p_T above 10 GeV in the EB ECAL,
- at least one loose photon with p_T above 80 GeV in the EB ECAL and separated by $\Delta R = \sqrt{(\Delta\phi)^2 + (\Delta\eta)^2} > 0.8$ from the leading electron.

6.2.1 Primary Vertex

All events considered in the analysis are required to have at least one good primary vertex. The criteria for a good primary vertex are as follows:

- The number of degrees of freedom for the vertex fit χ^2 must be greater than or equal to four.

- The z-component of the vertex position should not be greater than twenty-four centimetres from the origin, $|z_{vertex}| < 24$ cm.

- The transverse component of the vertex position with respect to the beam line should not be greater than two centimetres from the origin, $\rho_{vertex} = \sqrt{x^2_{vertex} + y^2_{vertex}} < 2$ cm.

6.2.2 Hadronic Transverse Energy

The HLT definition for determining the hadronic transverse energy sum, H_T, is followed. It is defined as the sum of all jet p_T for jets with $p_T > 40$ GeV and $|\eta| < 3.0$. All events considered are required to have H_T greater than 450 GeV. As demonstrated in Chapter 4, the offline trigger used is fully efficient above this cut. The H_T distribution of the data sample before any event selection is shown in Figure 6.2.

6.2.3 Tight Electron

The Electron/Gamma Physics Object Group's definition of a tight electron is followed in this analysis. The criteria are:

- $|\Delta\eta_{in}| < 0.004$,

- $|\Delta\phi_{in}| < 0.03$,

- $\sigma_{i\eta i\eta} < 0.01$,

- $H/E < 0.12$,

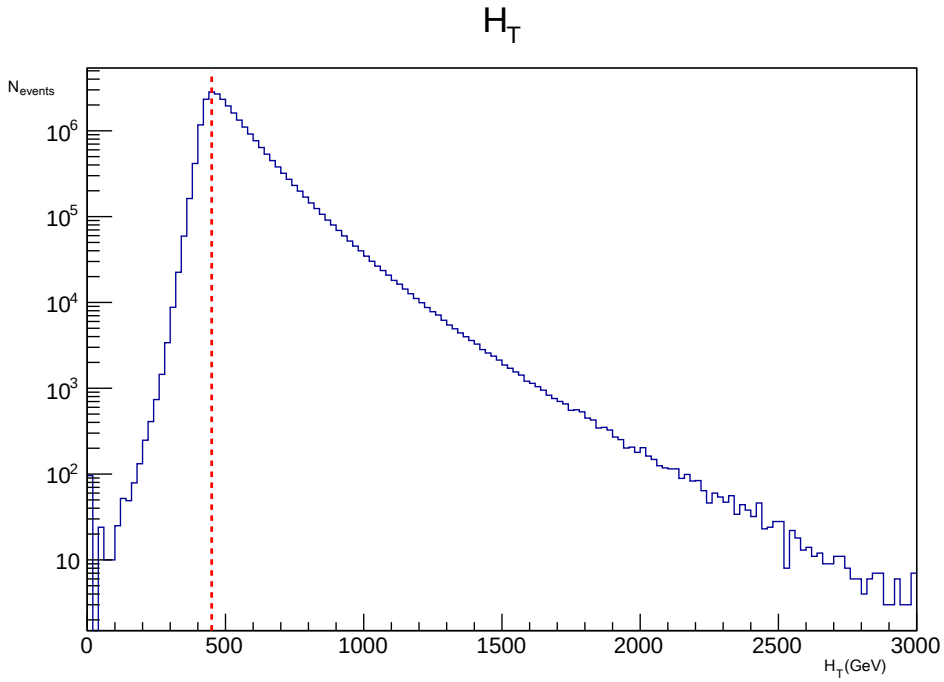

Figure 6.2: H_T distribution of events from the PhotonHad data with HLT and good primary vertex requirement.

- $|d_{xy}| < 0.02$ cm,
- $|d_z| < 0.1$ cm,
- $|1/E - 1/p_{in}| < 0.05$ GeV^{-1},
- combined relative isolation < 0.10,
- vertex fit probability < 0.000001,
- no missing hits in pixel detector,
- pass conversion veto.

The distributions of some of these variables are shown in Figures 6.3 and 6.4 before any event selection. The corresponding N-1 distributions, the distribution of

the quantity of interest after applying all other ID requirement, are also shown.

The tight electron p_T distribution events from the PhotonHad dataset with HLT requirement are shown in Figure 6.5. The big bump around 70 GeV is due to the Photon70 leg of the HLT trigger and the similarity between a photon and electron object. An ECAL shower due to a photon can sometimes be incorrectly matched to a random track from a charged particle. This would result in the misidentification of the photon as an electron. The other broader bump around 200 GeV is due to the PFHT400 or PFNoHT400 leg of the HLT trigger. Requiring high H_T in the trigger is equivalent to requiring jets. Some of these jets can be identified as electrons, especially if the jet is relatively isolated.

6.2.4 Loose Photon

The Electron/Gamma Physics Object Group's definition of a loose photon is followed in the analysis. The criteria are:

- Number of pixel seeds = 0,
- single tower $H/E < 0.05$,
- $\sigma_{i\eta i\eta} < 0.012$,
- ρ corrected PF charged hadron isolation < 2.6,
- ρ corrected PF neutral hadron isolation$< 3.5 + 0.04\,\rho_{PU}\,p_T$,
- ρ corrected PF photon isolation $< 1.3 + 0.005\,\rho_{PU}\,p_T$.

The distributions of some of these variables are shown in Figures 6.6 and 6.7 before any event selection. The corresponding N-1 distributions are also shown in these figures.

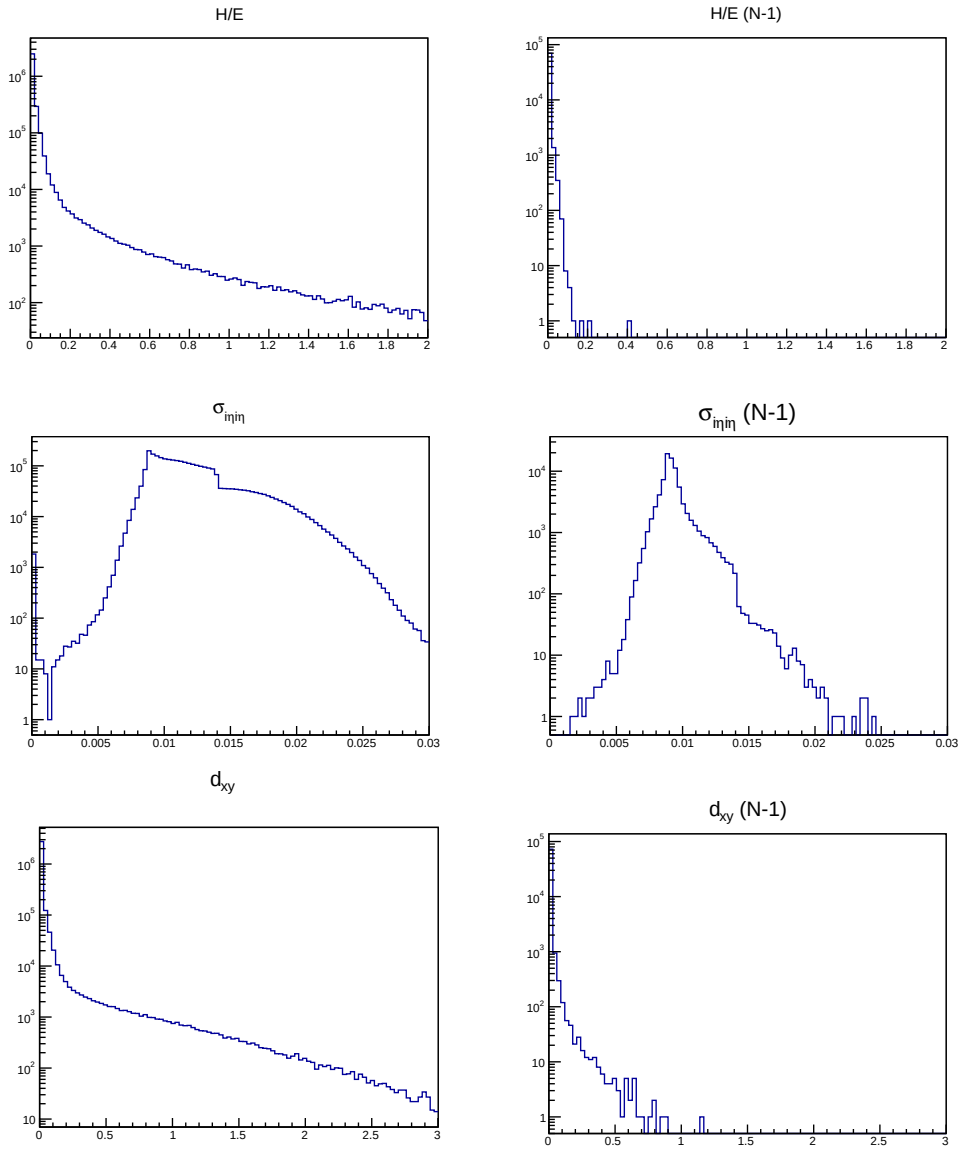

Figure 6.3: Electron variables of events from the PhotonHad data with HLT and good primary vertex requirement (left) and after applying the tight electron ID requirements except for the quantity of interest (N-1) (right): H/E (top), $\sigma_{i\eta i\eta}$ (middle) and d_{xy} (bottom).

The loose photon p_T distribution of Photonhad events with HLT requirement is shown in Figure 6.8. The big bump around 70 GeV is due to the Photon70 leg of the HLT trigger used. The other bump above 200 GeV is due to the PFHT400 or

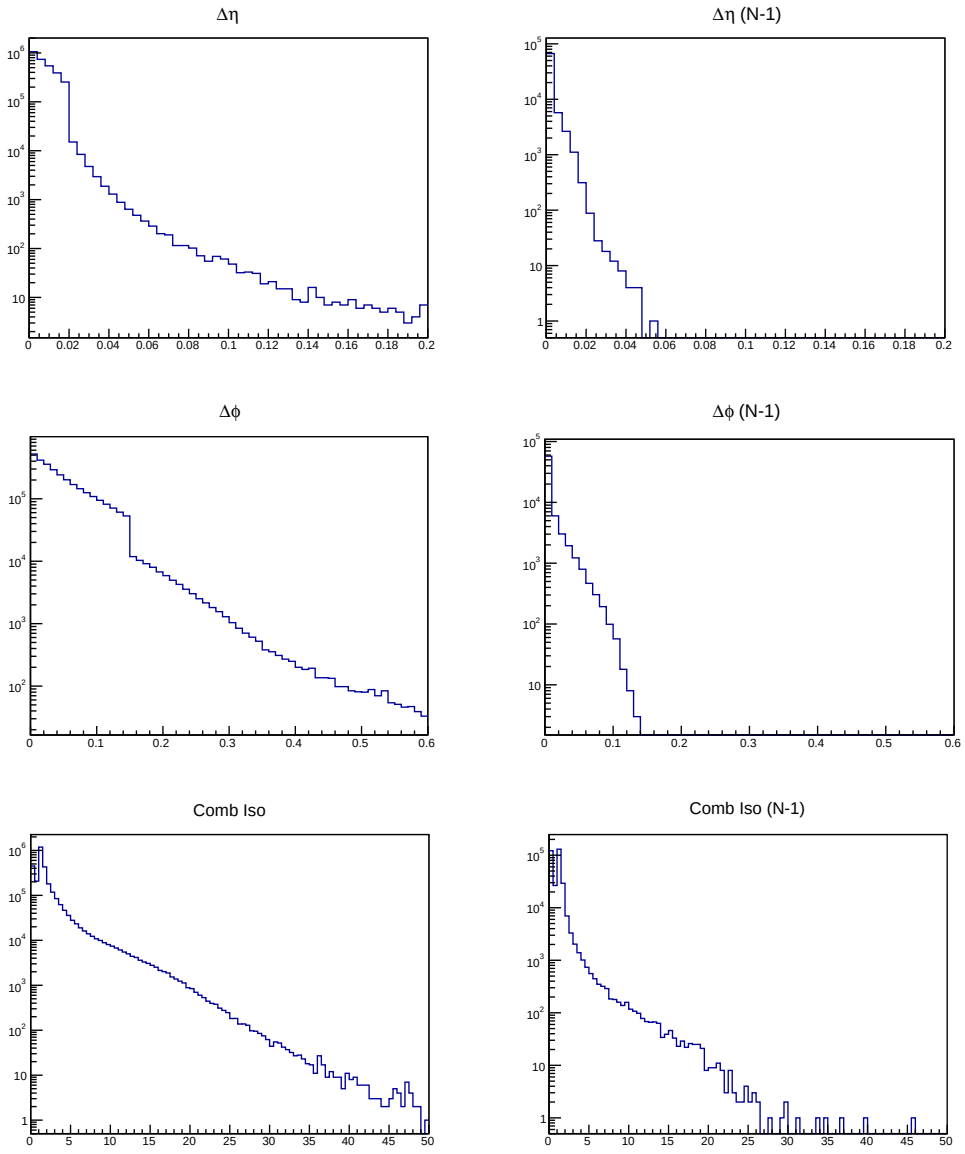

Figure 6.4: Electron variables of events from the PhotonHad data with HLT and good primary vertex requirement (left) and after applying the tight electron ID requirements except for the quantity of interest (N-1) (right): $\Delta\eta$ (top), $\Delta\phi$ (middle) and combined relative isolation (bottom).

PFNoHT400 leg of the HLT trigger which implicitly requires jets. Some of these jets can also be identified as photons, especially if a jet is relatively isolated and consists mainly of neutral mesons like π^0 or η.

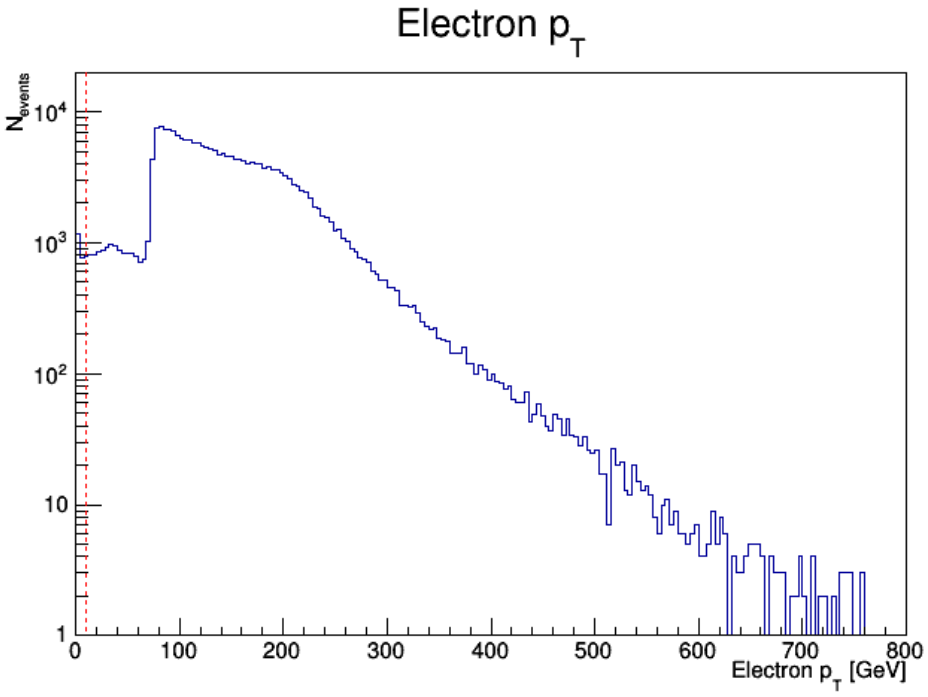

Figure 6.5: Tight electron p_T distribution of events from the PhotonHad dataset with HLT requirement.

6.3 Event Counts

The PhotonHad dataset consists of 24,015,752 events that pass the HLT triggers used in this study. Only 18,427,678 of these events pass the $H_T > 450$ GeV requirement. After requiring at least one loose photon passing the kinematics cuts only 660,721 events remain. This number drops to 1579 after requiring at least one tight electron in addition to the previous cuts.

Further requiring that the invariant mass of the photon and the electron is outside the 86 to 96 GeV mass window reduces the event count to 1405. The purpose of this requirement is to reduce the contribution of $Z \rightarrow ee$ events, where one e fakes a photon. Finally, to suppress final state radiation (FSR) and bremsstrahlung events, the ΔR between the photon and electron is required to be greater than 0.8. This

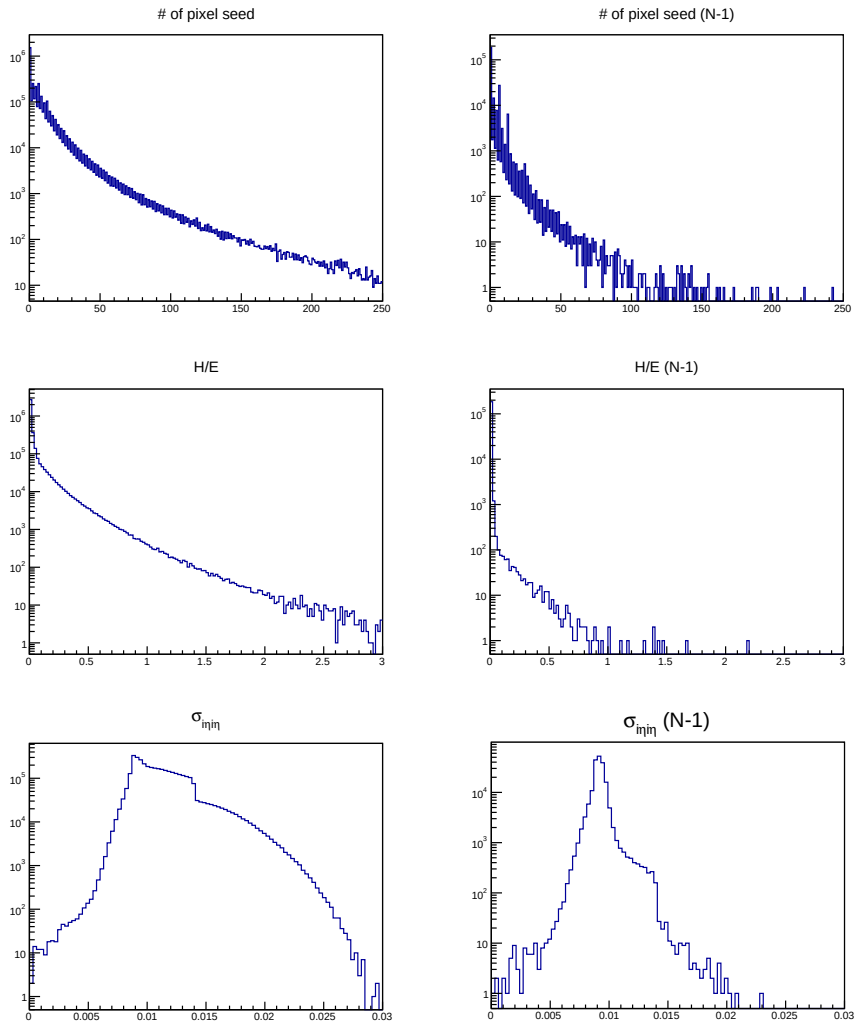

Figure 6.6: Photon variables of events from the PhotonHad data with HLT and good primary vertex requirement (left) and after applying the loose photon ID requirements except for the quantity of interest (N-1) (right): number of pixel seeds (top), H/E (middle) and $\sigma_{i\eta i\eta}$ (bottom).

reduces the final event count to 925.

The succession of cuts and the remaining number of events left are summarized in Table 6.1.

The loose photon p_T distribution of events that pass the criteria summarized in Table 6.1 is shown in Figure 6.9. The bump that was seen around 220 GeV before

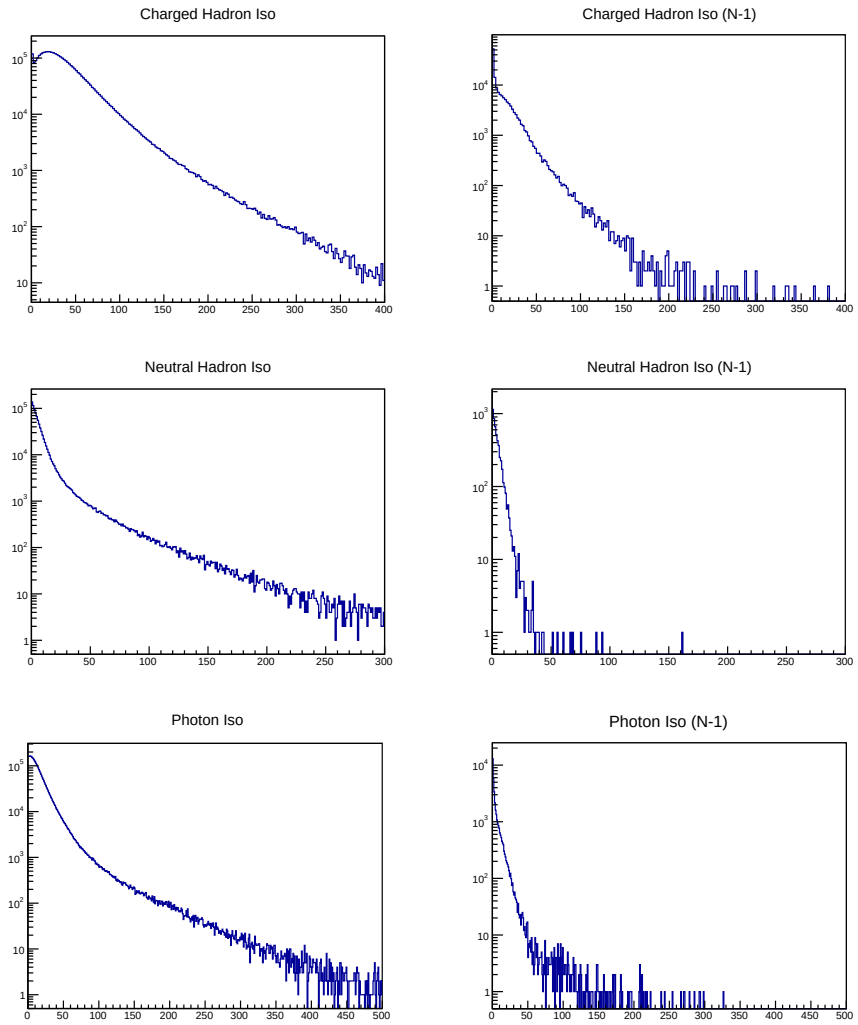

Figure 6.7: Photon variables of events from the PhotonHad dataset with HLT and good primary vertex requirement (left) and after applying the loose photon ID requirements except for the quantity of interest (N-1) (right): charged hadron isolation (top), neutral hadron isolation (middle) and photon isolation (bottom).

applying the event selection criteria (see Figure 6.8) is largely dampened but is still visible. This means that the event selection is not sufficient in rejecting jets that are misidentified as loose photons. The number of events containing jets that are misidentified as loose photons will be estimated using a data-driven technique and is discussed in Chapter 7.

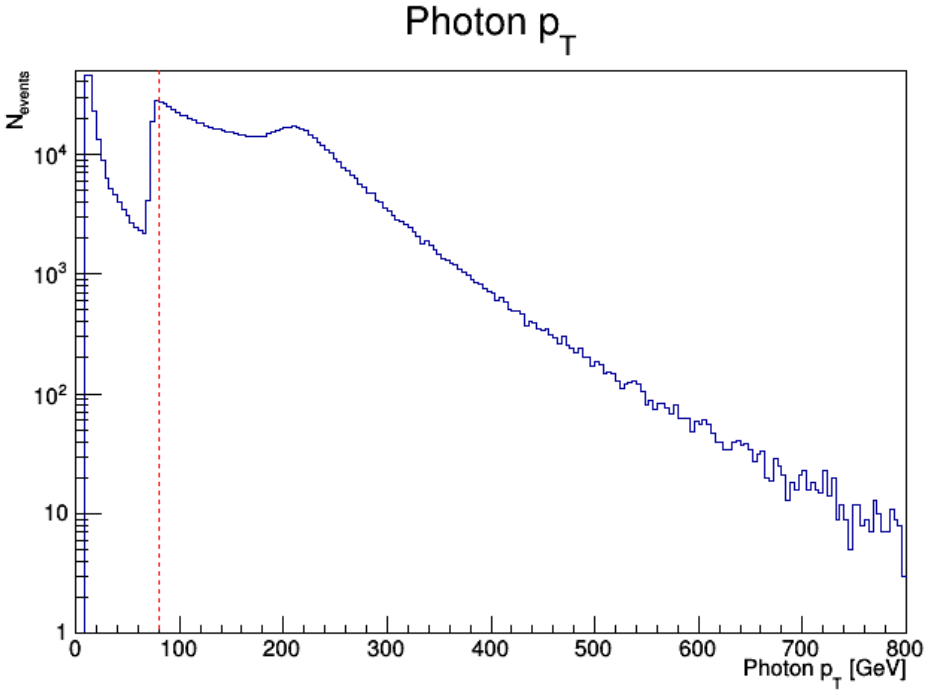

Figure 6.8: Loose photon p_T distribution of events from the PhotonHad dataset with HLT requirement.

	Number of Events
PhotonHad Dataset	24,015,752
HT >450 GeV	18,427,678
at least one loose γ with $p_T > 80$ Ge V	660,721
at lease one e with $p_T > 10$ GeV	1579
$m_{e\gamma} > 96$ GeV or $m_{e\gamma} < 86$ GeV	1405
$\Delta R_{e\gamma} > 0.8$	925

Table 6.1: Event selection criteria and corresponding event counts.

The tight electron p_T distribution of the events that pass the criteria summarized on Table 6.1 is shown in Figure 6.10. The big bump that existed around 70 GeV before applying the event selection criteria is gone (see Figure 6.5). This is largely due to the cut on $m_{e\gamma}$ and $\Delta R_{e\gamma}$. Most of the photons that are misidentified as electrons are rejected by the selection cuts employed. The bump around 200 GeV that was

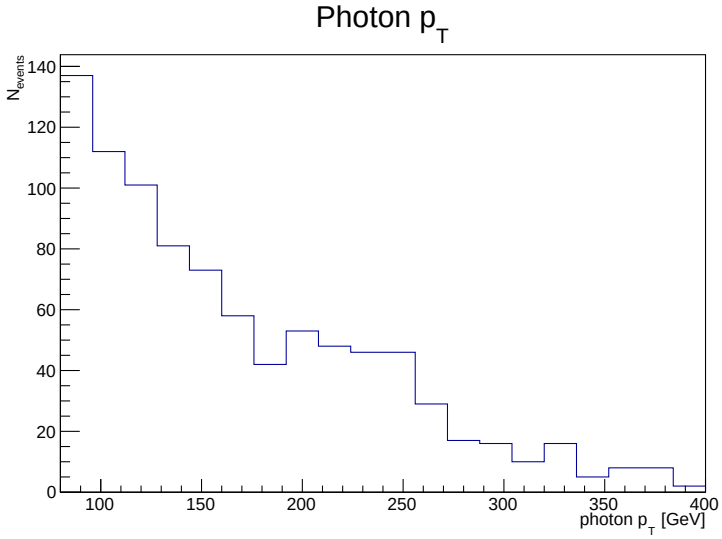

Figure 6.9: Loose photon p_T distribution of events from the PhotonHad dataset after applying all event selection criteria.

seen before applying the event selection criteria (see Figure 6.5), though dampened, is still there. This means that the event selection is not sufficient in rejecting all jets that are misidentified as tight electrons. The number of events containing jets that are misidentified as tight electrons will be estimated using a data-driven technique as discussed in Chapter 7.

The H_T distribution of the events that pass the selection criteria summarized in Table 6.1 is shown in Figure 6.11.

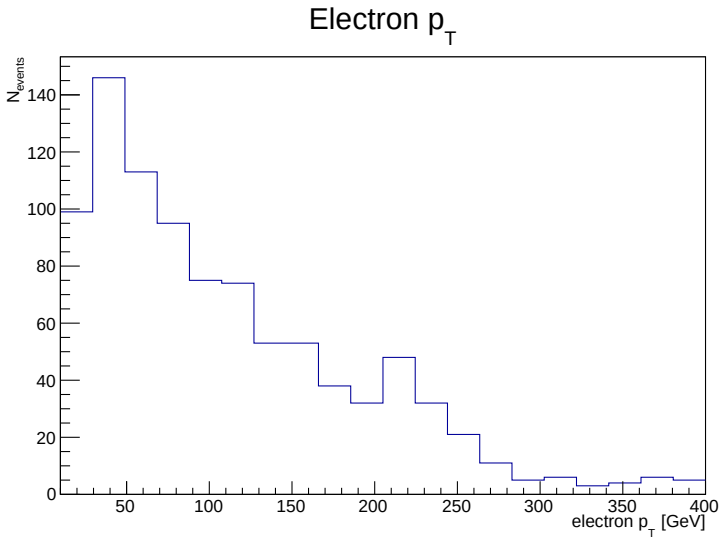

Figure 6.10: Tight electron p_T distribution of events from the PhotonHad dataset after applying all event selection criteria.

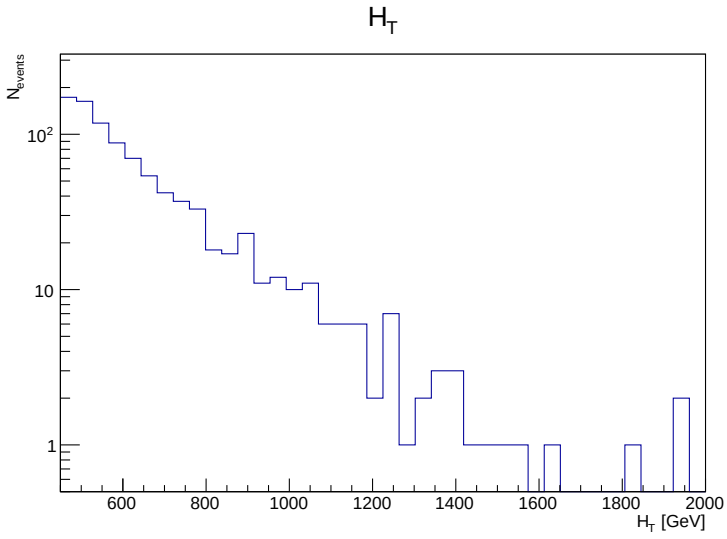

Figure 6.11: The H_T distribution of events from the PhotonHad dataset after applying all event selection criteria.

Chapter 7

Standard Model Backgrounds

As described in the previous chapter, some SM processes can also mimic the event topology described by MSSM events with GMSB and a wino-like NLSP with R-parity conservation. Such events will show up as backgrounds in this study. It is important to account for these backgrounds carefully, in order to draw firm conclusions on the existence or non-existence of the phenomenology that is sought for in this analysis.

Backgrounds are classified as irreducible and reducible. Irreducible backgrounds contain a real photon, electron and E_T^{miss}. These backgrounds will be estimated using MC samples. The dominant backgrounds for this study are standard model $W\gamma$ and the $t\bar{t}\gamma$ production, both of which are irreducible. Reducible backgrounds involve fake objects such as misidentified photons or electrons. Data-driven techniques will be used to estimate these background.

7.1 $W\gamma$ Background

As mentioned, $W\gamma$ is one of the dominant backgrounds of this study. In the $W\gamma$ events, the W boson can decay as $W \to e\nu_e$, resulting in an electron and a photon in

the final state. The electron neutrino would escape detection which would appear as E_T^{miss} in the event. Hence, this background has intrinsic E_T^{miss} and thus is irreducible. The final state of this process is very similar to the signal. To mitigate the impact of this background, a cut on the transverse mass between the electron and E_T^{miss}, defined as

$$M_T = \sqrt{2p_T E_T^{miss} \left(1 - \cos(\phi_e - \phi_{E_T^{miss}})\right)} \tag{7.1}$$

will be employed. The M_T distribution of the electron and E_T^{miss} from a $W\gamma$ process has a sharp edge close to the mass of the W boson. A cut above this region will decrease the efficiency of the SUSY signal but will drastically reduce the $W\gamma$ background. A sample M_T distribution of $W\gamma$ MC events together with signal SUSY MC is shown in Figure 7.1. As seen in the plot, a cut of $M_T > 120$ GeV is sufficient to reject the majority of $W\gamma$ events whereas only reducing the signal events by less than one-half.

The K-factor, which will be discussed more is Section 7.5.3, is estimated by doing a component fit in a control region. The K-factor is basically a correction factor that will approximately map a LO cross section to a NLO cross section. The MC samples used for the study of the $W\gamma$ background are

- WGToLNuG_PtG-50-130_8TeV-madgraph

- WGToLNuG_PtG-130_8TeV-madgraph

Comprising of a total of 3,000,000 and 471,458 MC events, respectively, and representing an integrated luminosity of 9.6 pb^{-1} and 0.3 pb^{-1}, respectively.

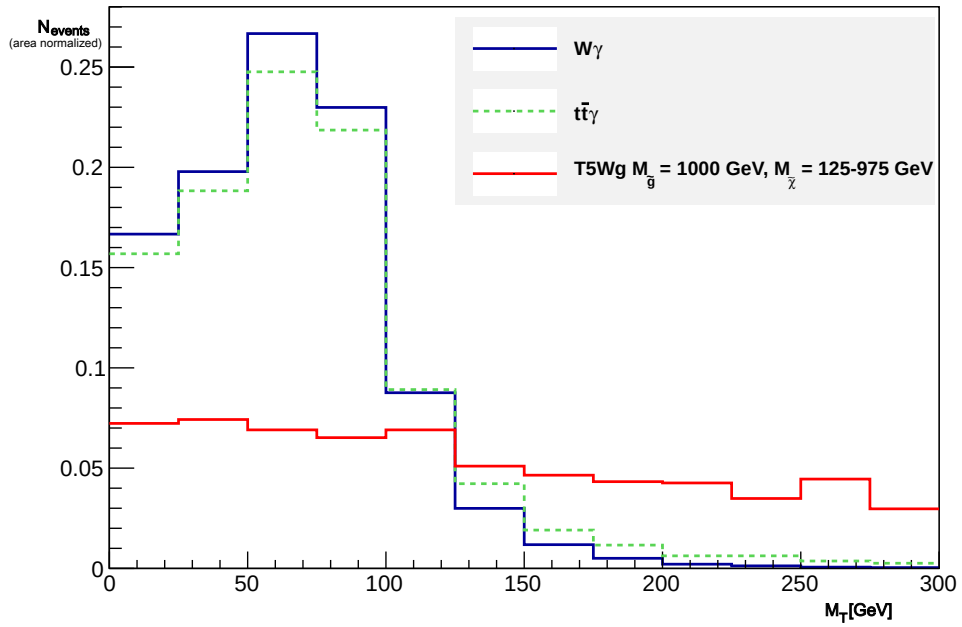

Figure 7.1: An area-normalized M_T distributions of electron and E_T^{miss} from $W\gamma$ MC (blue), $t\bar{t}\gamma$ (green) and signal MC (red), after full event selection.

7.2 $t\bar{t}\gamma$ Background

Like the $W\gamma$ background, radiative top quark pair production, $t\bar{t}\gamma$, is another dominant background in this study. In other studies with a similar final state selection [54–56], $t\bar{t}\gamma$ has a negligible contribution but the high H_T requirement of this analysis reduces other backgrounds and as a consequence increases the $t\bar{t}\gamma$ background relative to the other backgrounds especially at large E_T^{miss}. Like the $W\gamma$ background, events from the $t\bar{t}\gamma$ process also have intrinsic E_T^{miss} and are irreducible. The E_T^{miss} is also due to neutrinos from leptonic W decays when the $t\bar{t}$ pair decays fully leptonically or semi-leptonically, $t \to W\,b, W \to l\nu$. This means that the M_T distribution for $t\bar{t}\gamma$ events also has a sharp edge above the mass of the W boson. A sample M_T distribution of a $t\bar{t}\gamma$ MC is also shown in Figure 7.1. Similar to $W\gamma$, a cut of $M_T > 120$ GeV

is sufficient to reject the majority of $t\bar{t}\gamma$ events whereas only reducing signal events by less than a half. A cut of $M_T > 120$ GeV will be employed in the analysis.

The K-factor (see Section 7.5.3) again will be estimated by a component fit in a control region. The specific MC sample used for determining the $t\bar{t}\gamma$ background is TTGJets_8TeV-madgraph, comprising a total of 1,791,552 MC events.

7.3 $e \to \gamma$ Fake Background

Mis-reconstructed electrons can be identified as photons. Most of these misidentified photons involves $Z \to ee$ events where one electron fakes a photon resulting in an $e\gamma$ topology which is the same as the search topology. To measure the electron mis-identification rate, a proxy electron sample is used. A proxy electron is defined as a photon object passing all loose photon identification criteria except for the pixel veto. In the event selection the proxy electron takes the place of the photon in the event. Thus, instead of requiring a loose photon and a tight electron, a proxy electron and a tight electron is required. To determine the probability that a physical electron is identified as a photon a tag-and-probe method is used [40]. This $e \to \gamma$ misidentification probability is also referred to as fake rate and is expressed as:

$$f(e \to \gamma) = \frac{N_e^\gamma}{N_e^e + N_e^\gamma}, \tag{7.2}$$

where N_e^x is the number of physical electrons identified as x with $x = e, \gamma$. Proxy electrons represent N_e^e. In order to determine N_e^γ, which is the relevant quantity, Equation (7.2) can be used to obtain

$$N_e^\gamma = \frac{f}{1-f} N_e^e. \tag{7.3}$$

The term $\frac{f}{1-f}$ is called the transfer factor or scale factor and is expressed as a function of p_T of the proxy electron. For proxy electrons with $p_T > 80$ GeV, the fake rate is determined to be 0.0157 ± 0.0004.

7.4 Jet $\rightarrow \gamma$ Fake Background

Electromagnetically-fluctuating jets with few or no charged tracks but a high neutral fraction can be misidentified as photons. Although the probability for this occurrence is small due to the multiple layers of jet rejection, the jet production cross section is very large leading to a significant contribution of this background. Such jets faking photons are mostly isolated π^0 or η mesons decaying into two photons.

Since both the fragmentation of hadrons to photons and their subsequent showering might not be modeled well in the simulation, a data-driven method to estimate the contribution from such background events into the signal region is employed. The method works by scaling a sample of photon-like jets (hadron proxy objects) with the estimated ratio of the number of fake photons to the number of proxies (transfer factor). A proxy jet is defined as a loose photon with looser isolation cuts or a loose photon that fails the $\sigma_{i\eta i\eta}$ requirement. The transfer factor is derived as a function of the p_T of the proxy jet.

In particular, the estimation of the photon fake rate is performed in multiple steps. First, the fraction of hadronic fakes within the candidate photons is determined in a sample where the photons are free of trigger constraints. This fraction is subsequently applied to the sample of candidate photons in a control region to construct the estimation of the p_T distribution of the hadronic fakes. The ratio of this p_T distribution to the distribution of the hadron proxy objects is then taken to obtain the transfer factor as a function of p_T. Finally, the obtained function is used to weight the hadron

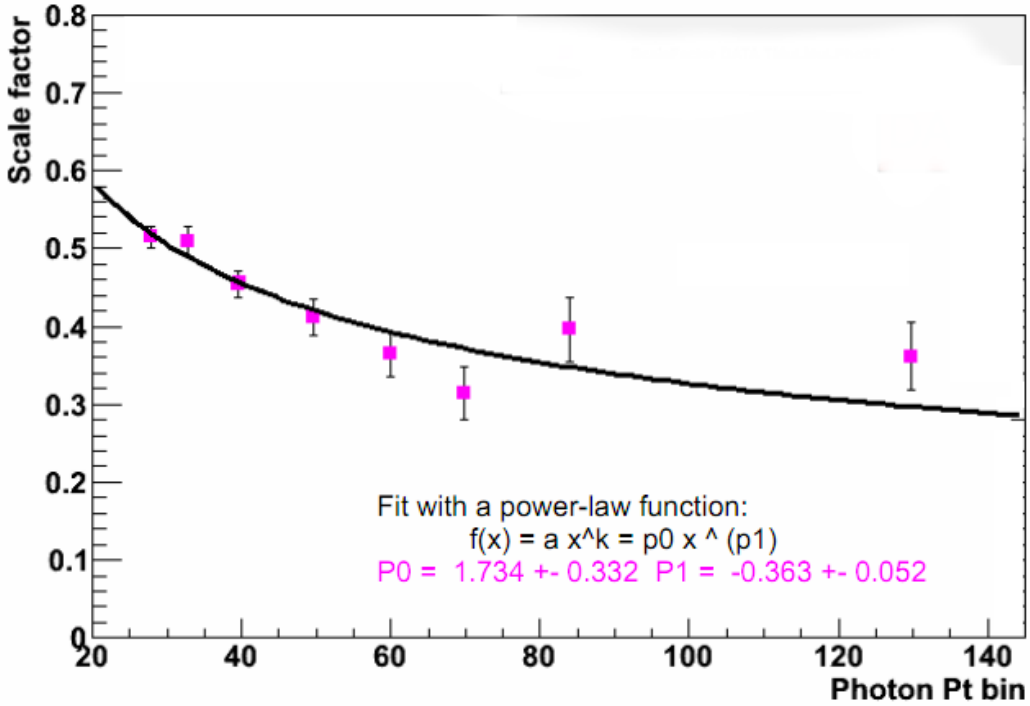

Figure 7.2: Distribution of the transfer factor from the determination of the jet $\rightarrow \gamma$ fake rate.

proxy sample. The result of this procedure is shown as the estimated transfer factor of the jet to photon fake rate versus p_T in Figure 7.2.

7.5 Jet/$\gamma \rightarrow e$ Fake Background

The total proton-proton cross section at the LHC is dominated by hard-scattering processes produced by the strong interaction. These processes are often called QCD or multi-jet events since their final states are dominated by jets. Photons along with jets can also appear in QCD final states. Although processes with photons are suppressed by the electromagnetic coupling constant, and further reduced by the large photon p_T requirement due to the trigger threshold, the QCD production at the LHC is huge. In principle, QCD events have a very small contribution from undetectable particles.

Thus, the intrinsic missing transverse energy is small for QCD events but can be caused by a mis-measured jet energy due to the limited jet energy resolution.

When jets are misidentified as electrons, QCD events with photons will appear as background to this study. Although the probability for this occurence is small, the QCD cross section is very large leading to a significant contribution of this background. To estimate the jet $\rightarrow e$ fake rate, the fakeable object method [57] will be utilized. The idea of this method is to use the ratio of the number of electrons identified as tight electrons to the number of electrons identified as loose electrons to estimate the number of fake electrons. This method will be discussed below.

7.5.1 Fakeable Object Method

The total number of electrons passing the loose electron identification criteria, N_{loose}, is made up of N_{prompt} prompt and real electrons and N_{fake} fake electrons. N_{loose} is also the sum of the number of electrons passing the tight criteria, N_{tight}, and the number of electrons failing the tight criteria, $N_{failtight}$. N_{prompt} and N_{fake} are not directly measurable. However, they are related to N_{tight} and $N_{failtight}$, which can be determined directly from the data. It is an assumptions that all real prompt electrons will pass the tight electron ID criteria. However, most of the fake electrons will fail the tight electron ID criteria but a small fraction will survive. The following equations summarize the aforementioned relations.

$$N_{loose} = N_{prompt} + N_{fake} = N_{tight} + N_{failtight}, \tag{7.4}$$

$$N_{tight} = N_{prompt} + fN_{fake}, \tag{7.5}$$

$$N_{failtight} = (1 - f)N_{fake}. \tag{7.6}$$

In these equations, f is the "fake ratio", which is the probability for a fake electron passing the loose criteria to also pass the tight criteria. The ratio f depends on the electron p_T and can be interpreted as average over the fake electron spectra. It can also be used as an event by event weight over the fake electron proxy data. This ratio can be determined from QCD or other fake-lepton rich events as a function of the lepton kinematics. As mentioned above, it is not known which electrons are fake or prompt but only the number of electrons passing the tight criteria N_{tight} and electrons failing the tight criteria $N_{failtight}$ can be measured. From Equations (7.1) to (7.3), N_{prompt} and N_{fake} can be derived from the measurable quantities:

$$N_{promt} = \frac{1}{1-f}[(1-f)N_{tight} - fN_{failtight}], \tag{7.7}$$

$$N_{fake} = \frac{1}{1-f}N_{failtight}. \tag{7.8}$$

The number of signal events is then given by $N_{signal} = N_{prompt}$ and the number of fake events passing the tight electron ID cuts by $N_{contam} = fN_{fake}$. The factor f can be used as weights applied to individual electron distributions. It should be emphasized that not only N_{signal} , but also N_{contam} is important to estimate, as the latter provides a handle on the QCD background.

7.5.2 Determining the Fake Ratio

To determine the fake ratio, f, a QCD Monte Carlo sample is used: QCD_Pt-15to3000_TuneZ2star_Flat_8TeV_pythia6. The definition for a tight electron is the same as the definition of the tight electron selection used for the electron signal. The loose electron has a looser cut on $dz > 0.2$ cm and a combined relative isolation greater than 0.6. To calculate the fake ratio, both the tight electron and the loose

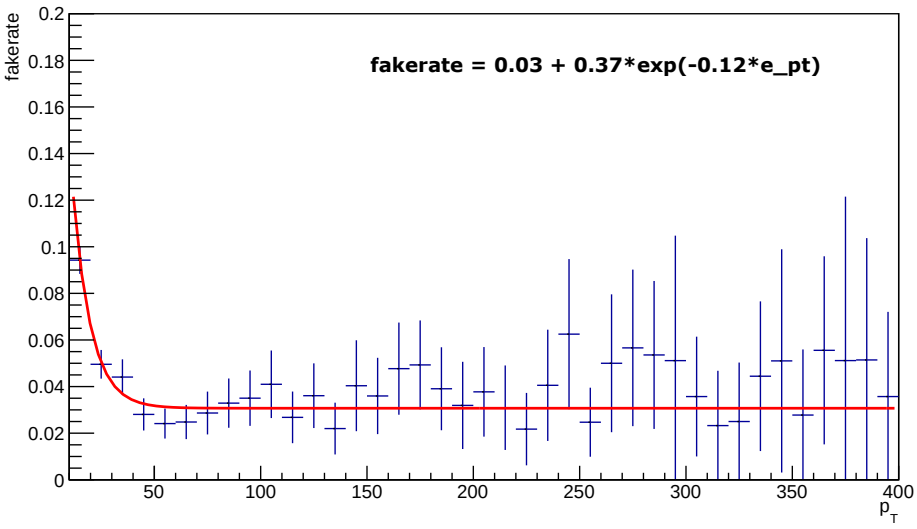

Figure 7.3: Electron fake ratio, which is the ratio of tight electron p_T over loose electron p_T.

electron p_T distributions were determined from the QCD MC sample above. The tight electron p_T distribution is then divided by the loose electron p_t distribution. The resulting distribution is then fitted to the following empirical function,

$$f(p_T) = a + b\exp(-c\,p_T) \tag{7.9}$$

using a least-squares fitting algorithm. The parameters a, b, and c are determined by minimizing the sum of the squares of the residuals. As a result, the fake ratio is determined to be $f(p_T) = 0.03 + 0.37\exp(-0.12\,p_T)$ (see also Figure 7.3).

To test the computed fake ratio, the fakeable object method used to determine the jet/$\gamma \to e$ background was used to estimate the p_T, M_T and E_T^{miss} distribution of $t\bar{t}$ MC events that have no real and prompt electrons. The resulting distributions are then compared to the distribution determined using MC truth information where a real and prompt electron is defined as an electron coming from a Z boson, W boson,

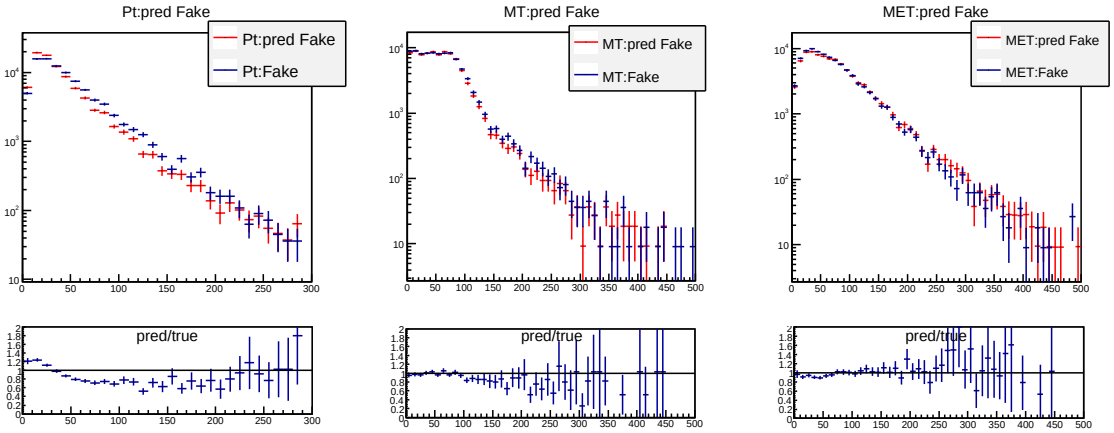

Figure 7.4: Closure of the electron fake ratio method using TTJets_TuneZ2star_8TeV-madgraph-tauola MC events and comparing the p_T (left), M_T (middle), and E_T^{miss} (right) distributions.

or τ lepton. Figure 7.4 shows such a comparison where it can seen that the prediction agrees well with the expected distribution.

When compared to a fake ratio determined using PhotonHad data a difference of almost a factor of three is seen. The shape of the distributions predicted using the fakeable object method is however similar to other methods in estimating the jet/$\gamma \rightarrow e$ background. To account for this difference a two-component fit method will be utilized and is discussed in the next section.

7.5.3 Scale Factors

The cross sections of the $W\gamma$ and $t\bar{t}\gamma$ MC samples are calculated only up to the leading order (LO) term. The information from the next-to-leading order (NLO) calculation can be encapsulated in the K-factor, which is the ratio of the NLO to LO cross section for a given process. To calculate the K-factor for the $W\gamma$ and $t\bar{t}\gamma$ MC samples a two-component fit method is used.

The first step of the two-component fit method is to pick a control region where

the signal rate is very low. In this analysis the control region is chosen to be $E_T^{miss} < 80$ GeV and $M_T < 120$ GeV. The target distribution is then defined as a variable in this control region where the contribution from known backgrounds are subtracted from the data. In this analysis, the M_T variable is used. In particular, the target distribution is the M_T from the PhotonHad control region minus the contribution of the $e \to \gamma$ and jet $\to \gamma$ backgrounds. The two remaining background distributions are then scaled to fit the target distribution. In this case, the remaining background distributions that will be scaled are (1) the jet/$\gamma \to e$ fakes and (2) the sum of the $W\gamma$ and $t\bar{t}\gamma$ backgrounds. The scale factors is determined by a least-squares fit. The resulting scale factors are shown as a function of M_T in Figure 7.5.

Using these scale factors, the stacked electron p_T, photon p_T, H_T, and M_T distributions using the various background determinations are compared in the control region to the corresponding distribution from the PhotonHad data (see Figures 7.6 and 7.7). It can be seen that the background is modelled well.

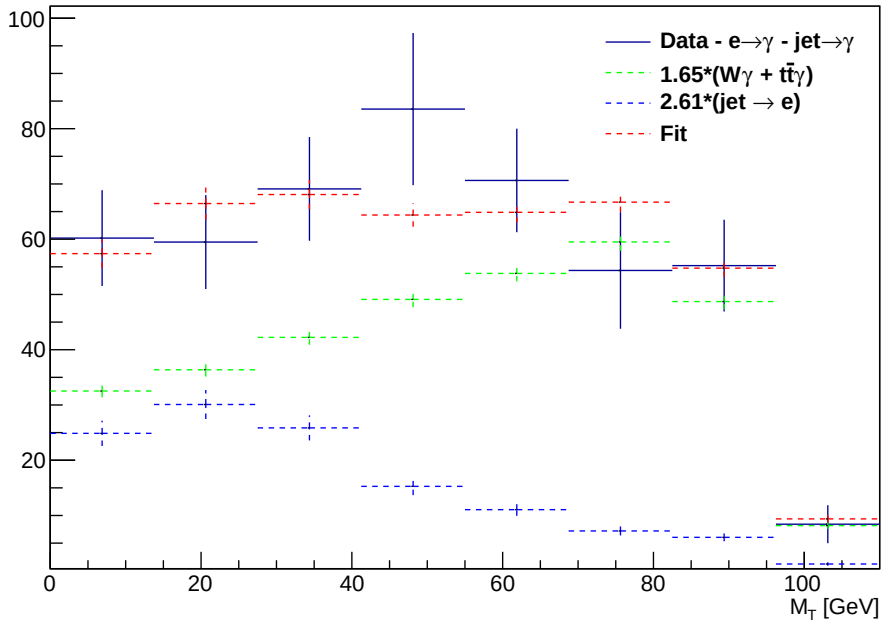

Figure 7.5: Distribution of the scale factor as a function of M_T.

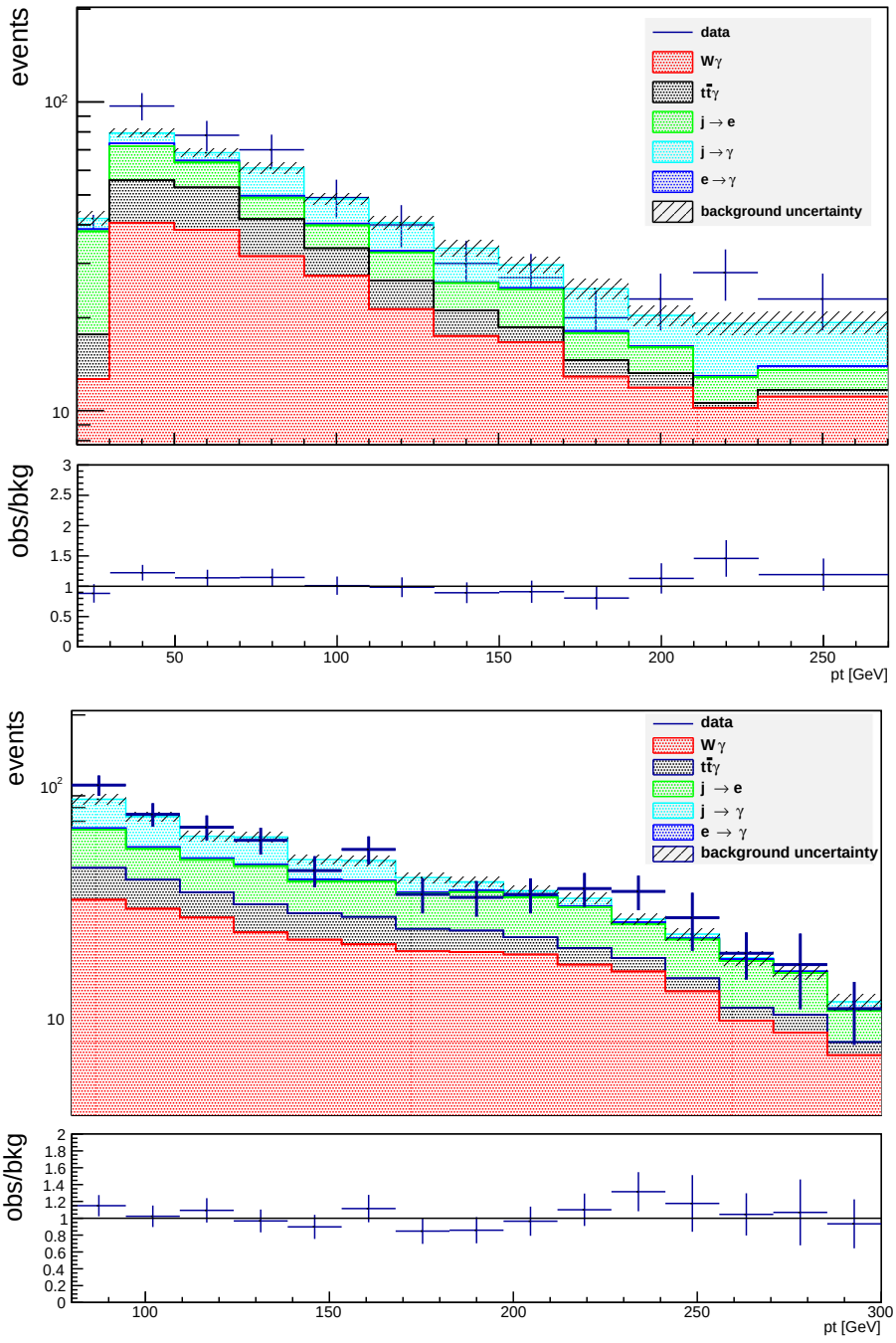

Figure 7.6: Electron p_T distribution (top) and Photon p_T distribution (bottom) for events with $E_T^{miss} < 80$ GeV and $M_T < 120$ GeV.

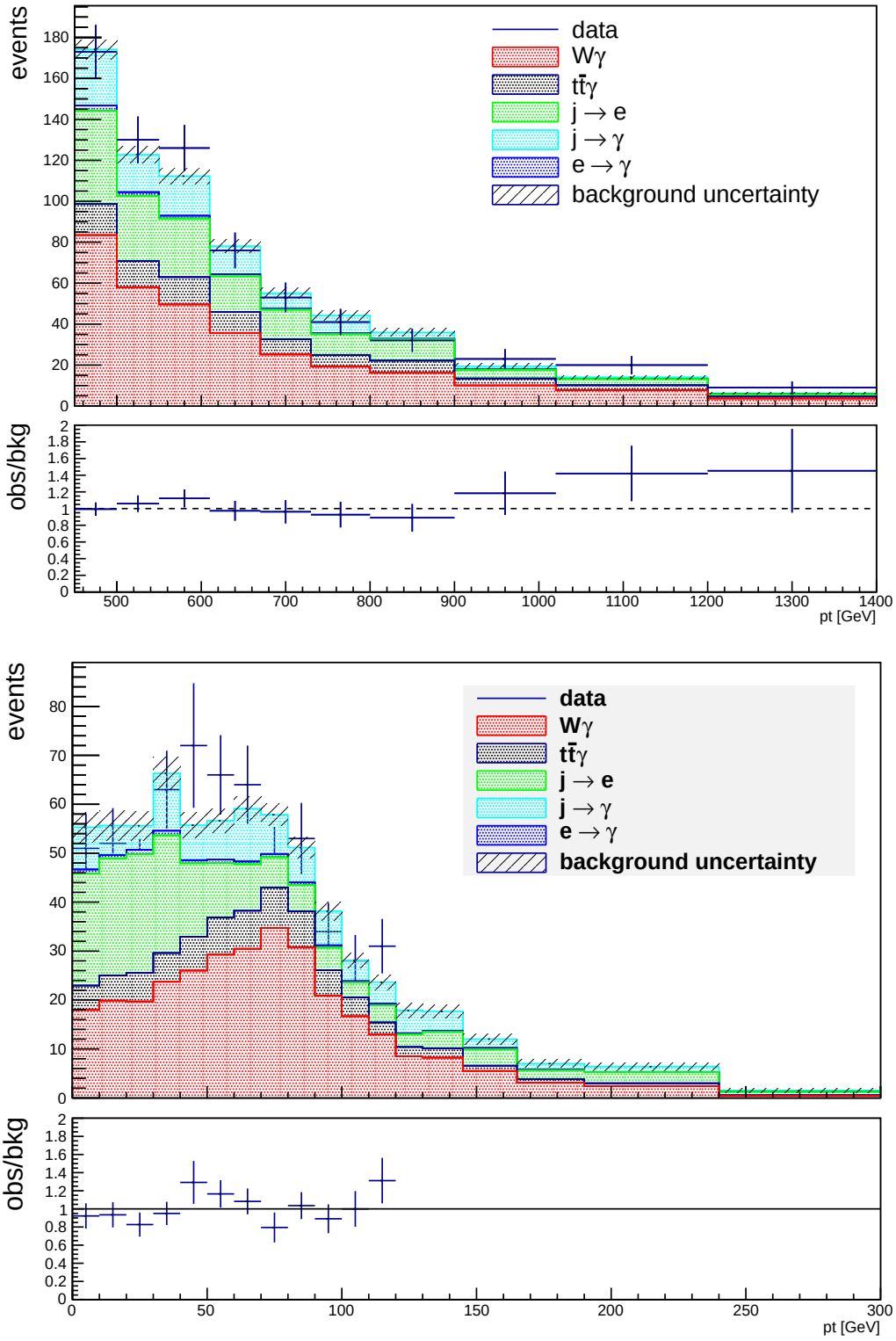

Figure 7.7: H_T distribution for events with $E_T^{miss} < 80$ GeV and $M_T < 120$ GeV (top) and blinded M_T distribution for events with $E_T^{miss} < 80$ GeV (bottom).

Chapter 8

Results

The E_T^{miss} distribution after applying the signal selection is shown in Figure 8.1 together with the sum of the expected background contributions. The E_T^{miss} distribution from a signal MC for gluino $\tilde{g}$ mass of 1000 GeV and neutralino/chargino $\tilde{\chi}$ mass of 625 GeV is also overlaid in the figure. The data agree well with the SM expectations and do not exhibit any evidence for an excess of events at high E_T^{miss}. The exact content of the last six bins in this distribution is summarized in Table 8.1. The six distinct bins have the following E_T^{miss} ranges in GeV: [100,130), [130,160), [160,200), [200,270), [270,350) and [350,∞). These same bin ranges will be used as the final signal region for the calculation of exclusion limits. This multi-channel counting experiment will be combined into a single limit. The CL_S method is used to determine 95% confidence level upper limits for a scan in the lightest neutralino/chargino versus gluino mass plane.

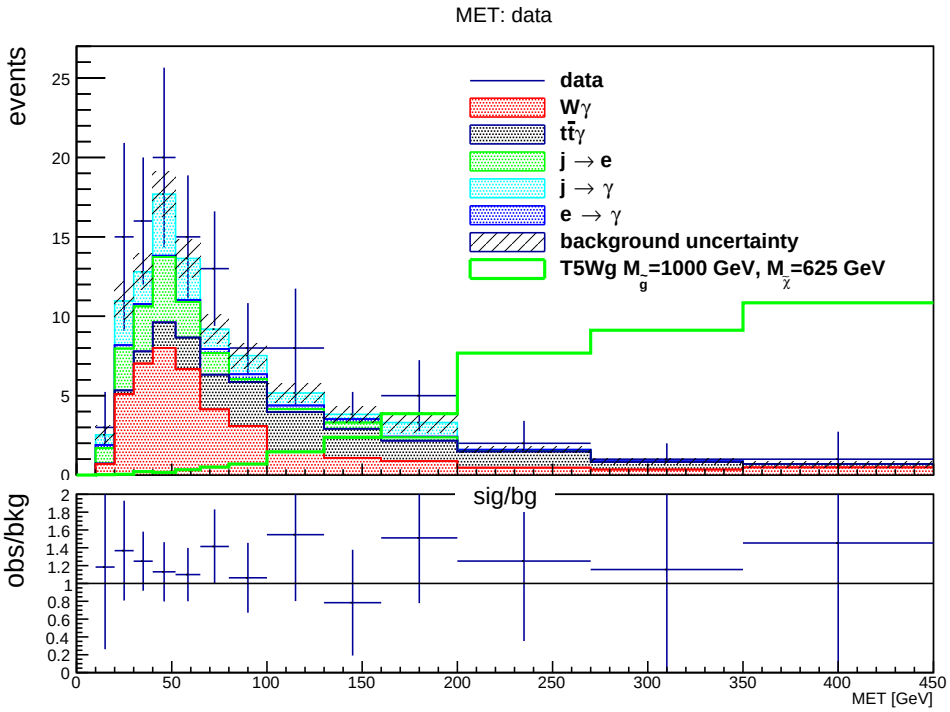

Figure 8.1: The E_T^{miss} distribution after all selection criteria.

Table 8.1: Number of events in the six highest MET bins.

	Bin 0	Bin 1	Bin 2	Bin 3	Bin 4	Bin 5
$W\gamma$	1.4	1.1	0.9	0.5	0.3	0.9
$t\bar{t}\gamma$	2.5	1.8	1.3	1.0	0.5	0.3
$e \to \gamma$	0.2	0.2	0.2	0.1	0.1	0.0
$j \to \gamma$	0.8	0.3	0.9	0.0	0.0	0.0
$j/\gamma \to e$	0.2	0.4	0.2	0.0	0.0	0.0
Total Backgroud	5.1	3.8	3.5	1.6	0.9	1.2
PhotonHad data	8.0	3.0	5.0	2.0	1.0	1.0

8.1 Simplified Model

In 2011 and 2012, many searches for new physics beyond the standard model (BSM) have been performed by the CMS experiment. No significant excess above the standard model prediction has been observed so far. Searches for BSM physics are very

different from the Higgs search, or the search for the top quark: there are many models with many parameters. Thus, the interpretation of search results is not trivial and making a meaningful comparison of different searches is almost impossible. For these reasons CMS decided to create simplified models as a basis for comparison. In a simplified model only a limited set of hypothetical particles and decay chains is introduced to describe the experimental results of a specific search channel. The main free parameters of a simplified model are the particle masses and the branching ratios. For this analysis, a simplified model will be used as a basis for setting the limits. In this simplified model pairs of gluinos are initially produced. One gluino decays to a quark-antiquark pair and an intermediate neutralino that decays to a photon and the LSP, and the second gluino decays to a quark-antiquark pair and a chargino that subsequently decays to a W boson and the LSP. The neutralino and chargino masses are set as degenerate to a common value to allow an interpretation in models of gauge mediation. The intermediate neutralino is labeled as the NLSP. A Feynman diagram of this model is shown in Figure 8.2. The process cross section for the simplified model is only dependent on the mass of the gluino $\tilde{g}$ as can be seen in Figure 8.4.

The simulated samples used in this search are produced as follows. Events are generated with the MADGRAPH 5 [58] event generator with up to two final state partons in addition to the primary new physics processes. The events are then passed to PYTHIA [59], which provides the parton shower process into jets. Because of the large number of individual simulated samples required to cover the simplified model parameter space scans, a fast detector simulation based on a full description of the CMS detector geometry and a parameterization of single-particle showers and response is utilized to reduce the computation time. Event pileup corresponding to the luminosity profile of the analyzed 2012 CMS data is added to all simulated

samples and the generated events are reconstructed using the same software program as for the collision data. For the signal Monte Carlo samples, uncertainties on the renormalization scale and parton distribution functions are considered. In addition, the difference between the leading order cross section calculation in MADGRAPH to the NLO calculation is expressed in form of a K-factor. These uncertainties including the K-factor are provided in a combined form by the LHC SUSY cross section working group and are taken into account in the limit setting procedure described below.

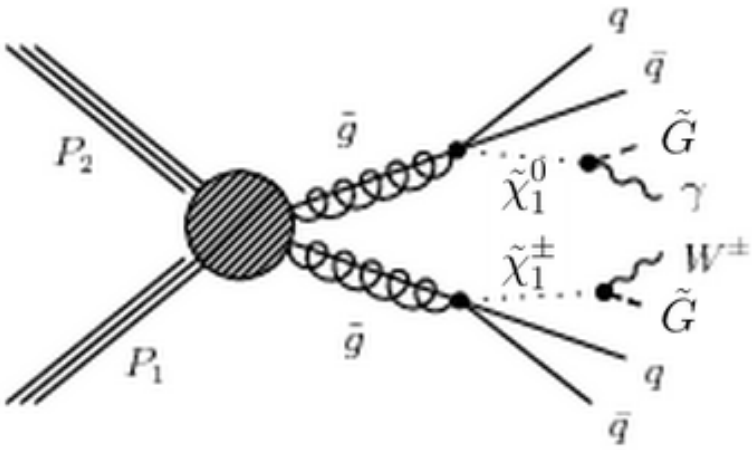

Figure 8.2: Feynman diagram illustrating the simplified model.

8.2 Calculation of 95% Confidence Level Limits

The CLs method used to determine the 95% confidence level (CL) limits is summarized here. This method is a modified frequentist method which utilizes nuisance parameters to construct a test statistics and generate pseudo-data for signal (s) and background (b) event counts. This search seeks to set limits on the signal production cross sections, and utilizes a signal strength modifier μ parameter. The signal and background yield predictions are subject to uncertainties which are introduced as nui-

Table 8.2: Summary of systematic uncertainties.

	Signal	$W\gamma$	$t\bar{t}\gamma$	$e \to g$	$j \to g$	$j/\gamma \to e$
Integrated luminousity	2.6%					
Cross section	15% - 35%					
K-factor		10%	10%			
Scale factor						50%
Transfer factor				10%	15%	

sance parameters θ. The signal and background predictions thus become functions of the nuisance parameters s(θ) and b(θ).

The sources of systematic uncertainties that affect the expected signal yield and background estimates are shown in Table 8.2. The uncertainty of the measured integrated luminosity is 2.6%. The uncertainty of the computed cross section for the signal MC samples varies from 15% to 35%. It increases as the mass of the gluino $\tilde{g}$ increases. The uncertainty on the scale factor used for the $j/\gamma \to e$ background was estimated by comparing the difference between the fake ratio determined using the QCD MC (see Section 7.5.2) and the PhotonHad dataset. The uncertainties of the transfer factor used for $j \to \gamma$ and $e \to \gamma$ are estimated by comparing the computed transfer factor to the transfer factor determined using the MC samples.

First a likelihood function $\mathcal{L}(\text{data}|\mu, \theta)$ is constructed,

$$\mathcal{L}(\text{data}|\mu, \theta) = \text{Poisson}(\text{data}|\mu \cdot s(\theta)) \cdot p(\tilde{\theta}|\theta), \tag{8.1}$$

where data represents the actual observation from data. Poisson(data|$\mu \cdot$ $s(\theta)$) stands for a product of Poisson probabilities to observe n_i events in bins i:

$$\prod_i \frac{(\mu s_i + b_i)^{n_i}}{n_i!} \exp -(\mu s_i + b_i). \tag{8.2}$$

To test the compatibility of the observed data with the background only or signal

plus background scenarios, where the signal is allowed to be scaled by some factor μ, the test statistics $\tilde{q}_\mu$ based on the profile likelihood ratio is constructed:

$$q_\mu = -2 \ln \frac{\mathcal{L}(\text{data}|\mu, \hat{\theta})}{\mathcal{L}(\text{data}|\hat{\mu}, \hat{\theta})}, \tag{8.3}$$

where $\hat{\theta}_\mu$ represents the conditional maximum likelihood estimators of θ for a given μ and the data. The $\hat{\mu}$ and $\hat{\theta}$ parameters correspond to the parameter estimators from the global maximum of the likelihood. The constraints $0 \leq \hat{\mu} \leq \mu$ are applied. The left hand side of the constraint is to ensure that the signal rate is positive, and the right hand side is imposed to ensure that upward fluctuations of the observed data are not interpreted as evidence against the signal hypothesis. The observed value of the test statistic $\tilde{q}_\mu^{obs}$ for a given μ is then calculated, along with the values of the nuisance parameters for the background only $\hat{\theta}_0^{obs}$ and background plus signal $\hat{\theta}_\mu^{obs}$ models which maximize the likelihood function defined in Equation (8.1). Simulation pseudo-data called "toys" are then generated to construct probability distribution functions (pdf) $f\left(\tilde{q}_\mu|\mu, \hat{\theta}_\mu^{obs}\right)$ and $f\left(\tilde{q}_\mu|0, \hat{\theta}_0^{obs}\right)$ from the background plus signal and background only models, respectively. The nuisance parameters are fixed to the values $\hat{\theta}_\mu^{obs}$ and $\hat{\theta}_0^{obs}$. The corresponding pdfs are used to construct probabilities representing the signal plus background p_μ and the background only p_b hypotheses:

$$p_\mu = P\left(\tilde{q}_\mu \geq \tilde{q}_\mu^{obs}|\text{signal} + \text{background}\right) = \int_{\tilde{q}_\mu^{obs}}^{\infty} f\left(\tilde{q}_\mu|\mu, \hat{\theta}_\mu^{obs}\right) d\tilde{q}_\mu, \tag{8.4}$$

$$1 - p_b = P\left(\tilde{q}_\mu \geq \tilde{q}_\mu^{obs}|\text{background only}\right) = \int_{\tilde{q}_0^{obs}}^{\infty} f\left(\tilde{q}_\mu|0, \hat{\theta}_0^{obs}\right) d\tilde{q}_\mu. \tag{8.5}$$

The value CL_s is defined as the ratio of these two probabilities:

$$\mathrm{CL}_s(\mu) = \frac{p_\mu}{1 - p_b}. \tag{8.6}$$

The $(1-\alpha)$ confidence level is defined as $\mathrm{CL}_s \leq \alpha$. Thus the observed 95% confidence level limit is found by varying μ to find $\mathrm{CL}_s = 0.05$.

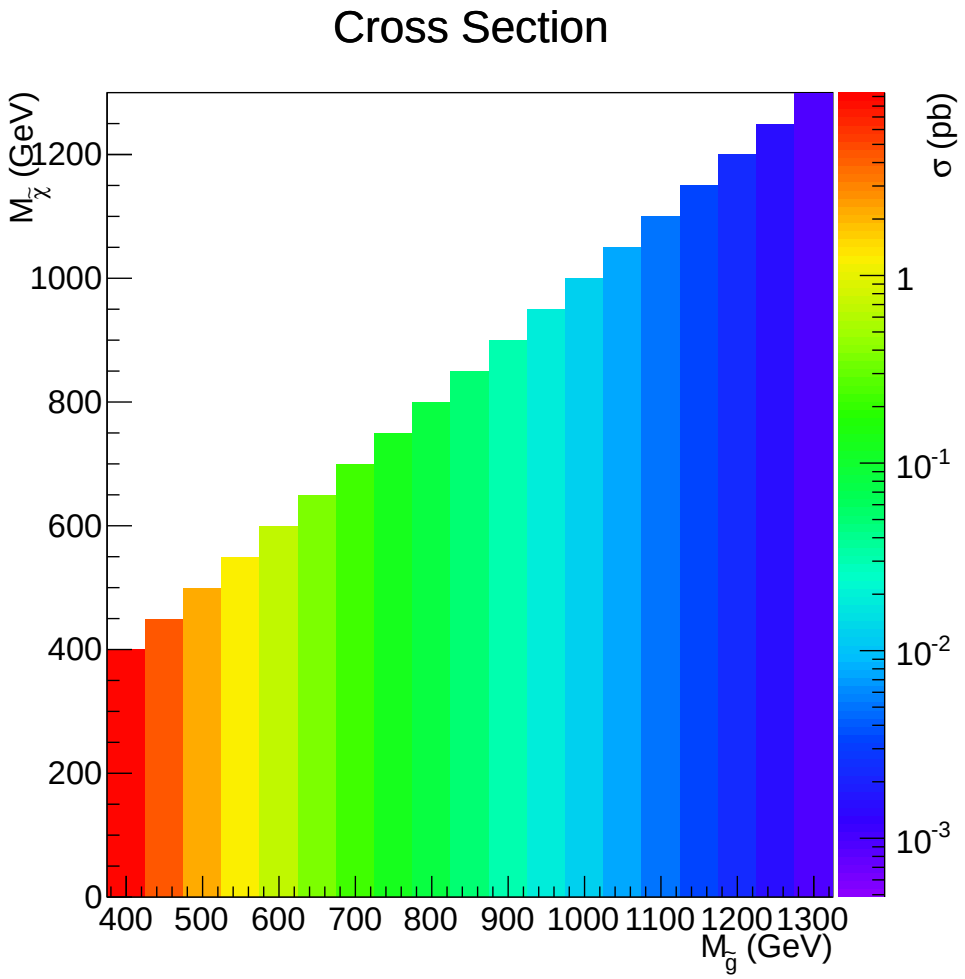

Figure 8.3: The theoretical production cross section of the simplified model signal scenario.

8.3 Upper Limits and Exclusion Regions

In order to determine the expected number of events for a given signal simulation point, the acceptance times efficiency is calculated. The scan is done over gluino $\tilde{g}$ masses from 400 GeV to 1300 GeV in steps of 50 GeV and for neutralino/chargino masses $\tilde{\chi}$ from 25 GeV to the corresponding mass of the gluino $\tilde{g}$ minus 25 GeV. The calculated acceptance times efficiency in the $\tilde{\chi}$ - $\tilde{g}$ plane is shown in Figure 8.4. From the figure, it can be seen that the acceptance increases as the mass of the gluino $\tilde{g}$ or the mass of the neutralino $\tilde{\chi}$ increases. With the acceptance times efficiency the 95% confidence level limit can be set over all points in the signal grid. The CL_S method [60] is used, in bins of E_T^{miss} ranges in GeV: [100,130), [130,160), [160,200), [200,270), [270,350) and [350,∞). This binned limit tool was developed by the CMS Higgs group and is widely used at CMS. The expected 95% CL cross section upper limit is shown in Figure 8.5. The observed 95% CL limit including the expected and observed exclusion contours is shown in Figure 8.6. It can be seen that gluino masses below 0.7 TeV for low chargino/neutralino masses up to 1.1 TeV for large NLSP masses are excluded. The obtained exclusion region is significantly better than the previous limits from analyses using the same final states [54, 55].

8.4 Summary

A search was performed for events with a photon with $p_T > 80$ GeV, an electron with $p_T > 10$ GeV and $E_T^{miss} > 100$ GeV using a data sample that corresponds to an integrated luminosity $\mathcal{L} = 19.6$ fb^{-1} of proton-proton collisions at $\sqrt{s} = 8$ TeV produced at the LHC and collected by the CMS detector. This is the first search with the photon and electron final state that has an implicit jet requirement through a cut

of $H_T > 450$ GeV on the total hadronic energy in the event. The number of events found is consistent with the expectation from SM backgrounds and no excess of events at high E_T^{miss} is observed. Such an excess of events could have been an indication for physics beyond the standard model. In the absence of an excess of events in the signal search region defined through $M_T > 120$ GeV and $E_T^{miss} > 100$ GeV, 95% CL exclusion regions are calculated for the production cross sections of SUSY particles in a simplified supersymmetry model. Gluino masses less than 720 GeV going up to 1 TeV for large chargino/neutralino masses are excluded. Previous analyses utilizing the same final state by the CMS and ATLAS experiments [54, 55], excluded gluino masses of less than 450 GeV and 619 GeV, respectively. The increased mass limits of this analysis compared to the previous ATLAS and CMS results are mainly due to the increased data sample available for this measurement but improvements to the search strategy also contributed.

Despite the negative result, the search for SUSY is not yet over. There is still a wide area in the parameter space of SUSY models that are not excluded. The LHC will run at a higher center-of-mass energy $\sqrt{s}$ in 2015, possible very close to the design $\sqrt{s}$ which is 14 TeV. This step-up in energy will result in much larger production cross sections for SUSY particles. It will also increase the energy range of all SUSY searches in CMS. These are good reasons to be optimistic about the possibility of still discovering SUSY at the LHC in the next few years.

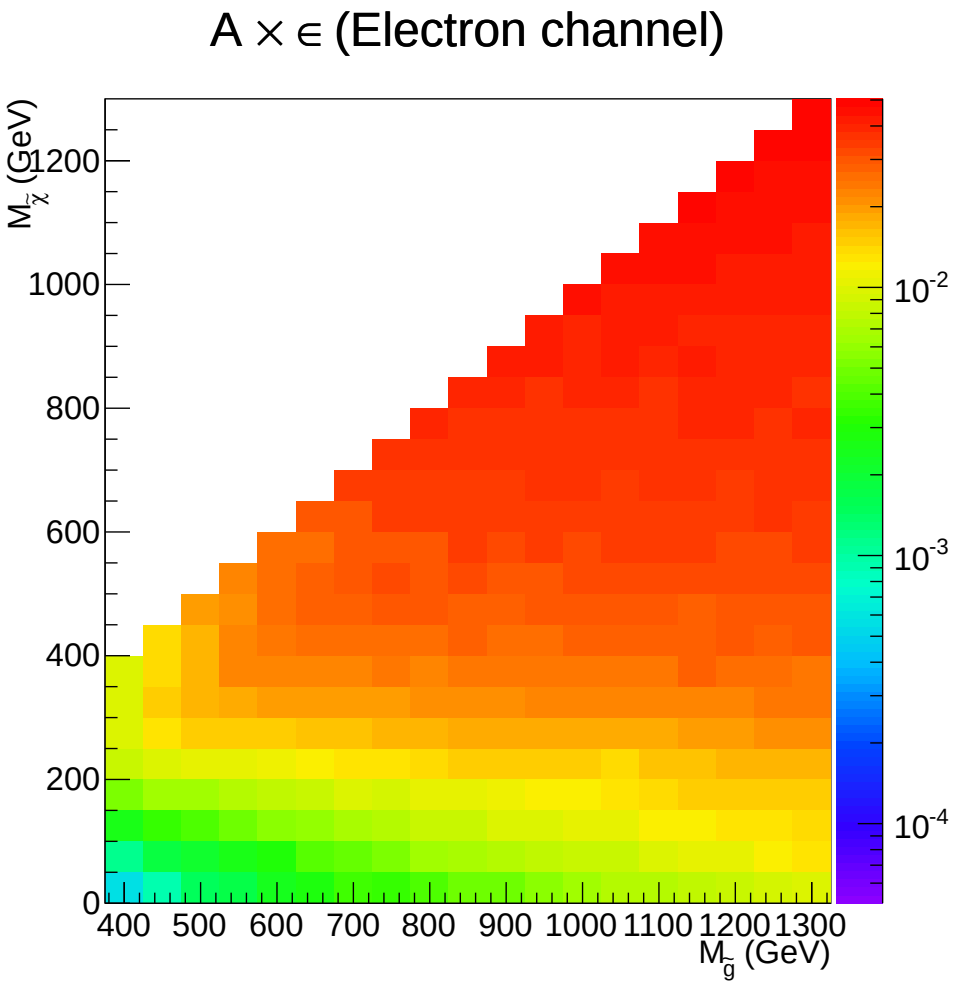

Figure 8.4: Acceptance times efficiency in the $\tilde{\chi}$-$\tilde{g}$ mass plane.

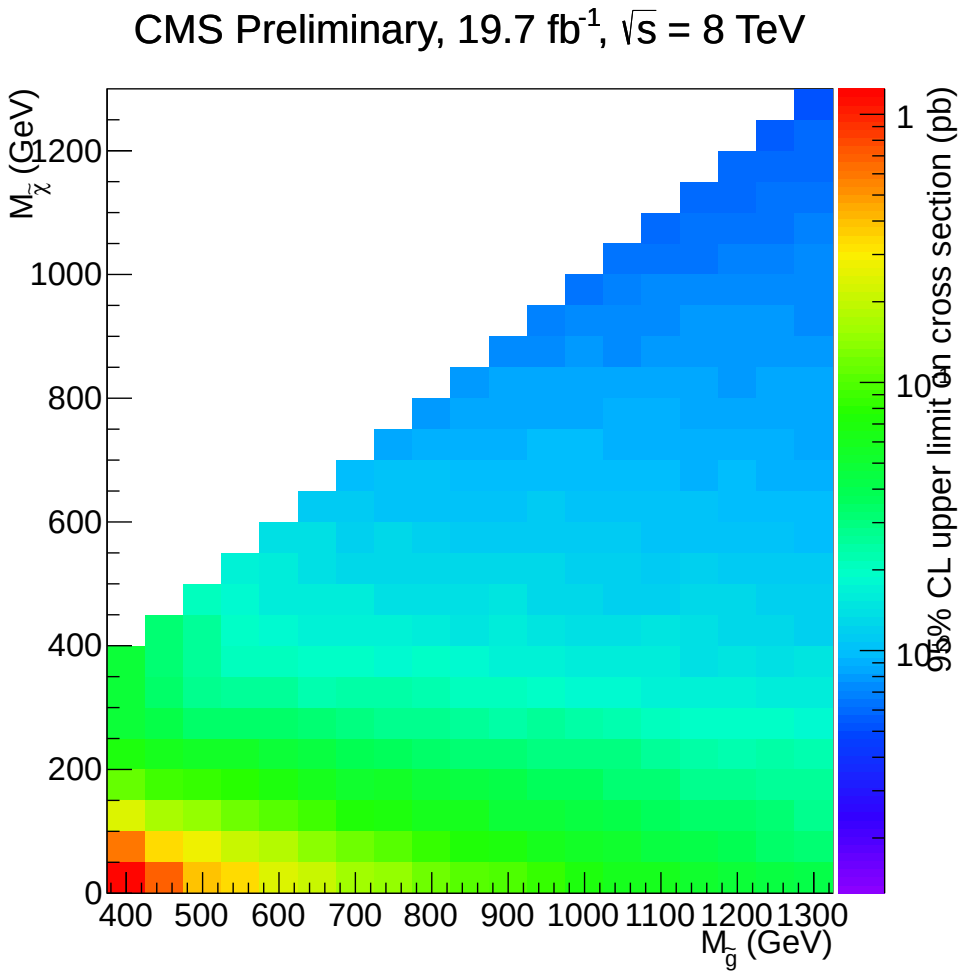

Figure 8.5: Expected 95% CL cross section upper limit in the $\tilde{\chi}$-$\tilde{g}$ mass plane.

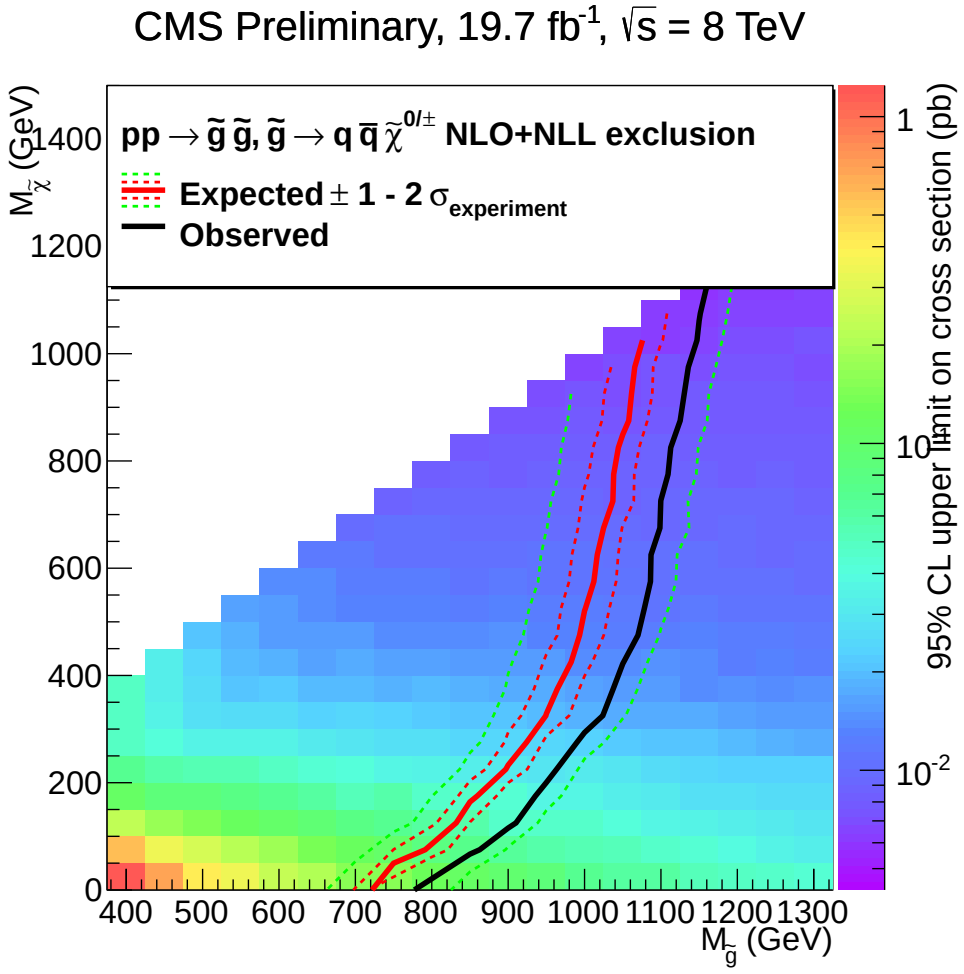

Figure 8.6: The observed 95% CL production cross section upper limits in the $\tilde{\chi}$-$\tilde{g}$ mass plane for the SUSY signal scenario.

Bibliography

[1] G. Arnison *et al.*, Physics Letters B **122**, 103 (1983).

[2] UA2 Collaboration, P. Bagnaia *et al.*, Phys. Lett. **B129**, 130 (1983).

[3] C. Campagnari and M. Franklin, Rev. Mod. Phys. **69**, 137 (1997).

[4] ATLAS Collaboration, G. Aad *et al.*, Phys. Lett. **B716**, 1 (2012).

[5] CMS Collaboration, S. Chatrchyan *et al.*, Phys. Lett. **B716**, 30 (2012).

[6] ALEPH Collaboration, CDF Collaboration, D0 Collaboration, DELPHI Collaboration, L3 Collaboration, OPAL Collaboration, SLD Collaboration, LEP Electroweak Working Group, Tevatron Electroweak Working Group, SLD Electroweak and Heavy Flavour Groups, arXiv:hep-ex/1012.2367 (2010).

[7] T. Aoyama, M. Hayakawa, T. Kinoshita, and M. Nio, Phys. Rev. **D77**, 053012 (2008).

[8] G. Gabrielse, New Measurement of the Electron Magnetic Moment and the Fine Structure Constant, in *APS Division of Atomic, Molecular and Optical Physics Meeting Abstracts*, p. 1001, 2007.

[9] M. Gell-Mann, Phys. Rev. **125**, 1067 (1962).

[10] Y. Ne'eman, Nucl. Phys. **26**, 222 (1961).

[11] A. Salam and J. C. Ward, Phys. Lett. **13**, 168 (1964).

[12] S. Weinberg, Phys. Rev. Lett. **19**, 1264 (1967).

[13] S. Glashow, Nucl. Phys. **22**, 579 (1961).

[14] P. W. Higgs, Phys. Rev. Lett. **13**, 508 (1964).

[15] J. H. Schwarz, NATO Adv. Study Inst. Ser. C. Math. Phys. Sci. **566**, 143 (2001).

[16] A. Ashtekar, Quantum Geometry and Gravity: Recent Advances, in *16th International Conference on General Relativity and Gravitation (GR16)*, pp. 28–53, 2013, arXiv:gr-qc/0112038.

[17] S. P. Martin *et al.*, *Perspectives on Supersymmetry II* (World Scientific Publishing Company, 2010).

[18] S. P. Martin, Adv. Ser. Direct. High Energy Phys. **21**, 1 (2010).

[19] V. Rubin, N. Thonnard, and J. Ford, W.K., Astrophys. J. **238**, 471 (1980).

[20] G. Jungman, M. Kamionkowski, and K. Griest, Phys. Rept. **267**, 195 (1996).

[21] D. Clowe *et al.*, Astrophys. J. **648**, L109 (2006).

[22] Planck Collaboration, P. Ade *et al.*, A&A, arXiv:1303.5062 (2013).

[23] MSSM Working Group, A. Djouadi *et al.*, arXiv:hep-ph/9901246 (1998).

[24] H. E. Haber, Nucl. Phys. Proc. Suppl. **62**, 469 (1998).

[25] Super-Kamiokande Collaboration, H. Nishino *et al.*, Phys. Rev. Lett. **102**, 141801 (2009).

[26] G. 't Hooft, Phys. Rev. Lett. **37**, 8 (1976).

[27] S. Dimopoulos, S. Raby, and F. Wilczek, Phys. Lett. **B112**, 133 (1982).

[28] G. R. Farrar and P. Fayet, Phys. Lett. **B76**, 575 (1978).

[29] S. Weinberg, Phys. Rev. **D26**, 287 (1982).

[30] P. Meade, N. Seiberg, and D. Shih, Prog. Theor. Phys. Suppl. **177**, 143 (2009).

[31] D. Marques, JHEP **0903**, 038 (2009).

[32] S. Abel, M. J. Dolan, J. Jaeckel, and V. V. Khoze, JHEP **0912**, 001 (2009).

[33] Y. Kats, P. Meade, M. Reece, and D. Shih, JHEP **1202**, 115 (2012).

[34] J. T. Ruderman and D. Shih, JHEP **1208**, 159 (2012).

[35] L. Evans and P. Bryant, JINST **3**, S08001 (2008).

[36] O. S. Bruning *et al.*, LHC Design Report: The LHC Main Ring (2004), CERN-2004-003.

[37] CMS Collaboration, G. Bayatian *et al.*, CMS Technical Design Report: Detector Performance and Software (2006), CERN-LHCC-2006-001, CMS-TDR-008-1.

[38] CMS Collaboration, G. Bayatian *et al.*, J. Phys. **G34**, 995 (2007).

[39] CMS Collaboration, S. Chatrchyan *et al.*, JINST **3**, S08004 (2008).

[40] CMS Collaboration, CERN Report No. CMS-PAS-EGM-07-001, 2010 (unpublished).

[41] R. Frühwirth, W. Waltenberger, and P. Vanlaer, CERN Report No. CMS-NOTE-2007-008, 2007 (unpublished).

[42] T. Speer, K. Prokofiev, R. Frühwirth, W. Waltenberger, and P. Vanlaer, CERN Report No. CMS-NOTE-2006-032, 2006 (unpublished).

[43] CMS Collaboration, CERN Report No. CMS-PAS-TRK-10-005, 2010 (unpublished).

[44] CMS Collaboration, M. Pioppi, CERN Report No. CMS Internal Note, 2008 (unpublished).

[45] T. Speer *et al.*, Nucl. Instrum. Meth. **A559**, 143 (2006).

[46] R. E. Kalman, Trans. ASME, D **82**, 35 (1960).

[47] CMS Collaboration, CERN Report No. CMS-PAS-EGM-10-004, 2010 (unpublished).

[48] D. Kovalskyi *et al.*, J. Phys. Conf. Ser. **219**, 032014 (2010).

[49] W. Adam, R. Frühwirth, A. Strandlie, and T. Todor, CERN Report No. CMS-NOTE-2005-001, 2005 (unpublished).

[50] R. Bellan, Nucl. Phys. Proc. Suppl. **177-178**, 253 (2008).

[51] CMS Collaboration, CERN Report No. CMS-PAS-MUO-10-002, 2010 (unpublished).

[52] CMS Collaboration, CERN Report No. PFT-10-01, 2010 (unpublished).

[53] M. Cacciari, G. P. Salam, and G. Soyez, JHEP **0804**, 063 (2008).

[54] ATLAS Collaboration, G. Aad *et al.*, ATLAS-CONF-2012-144 (2012).

[55] S. Chatrchyan *et al.*, Journal of High Energy Physics **6**, 93 (2011), 1105.3152.

[56] CDF Collaboration, A. Abulencia *et al.*, Phys. Rev. **D75**, 112001 (2007).

[57] CMS Collaboration, CERN Report No. AN2010/261, 2010 (unpublished).

[58] J. Alwall *et al.*, JHEP **1407**, 079 (2014).

[59] T. Sjostrand, S. Mrenna, and P. Z. Skands, JHEP **0605**, 026 (2006).

[60] A. L. Read, J. Phys. **G28**, 2693 (2002).